



This is to certify that the
thesis entitled

High Resolution Electron
Microscopy Examination of Dislocation
Core Structures in 52 Ni-Al Alloys
presented by

Scott Christopher Tann

has been accepted towards fulfillment
of the requirements for

M.S. degree in Materials Science

Major professor

Date 29 July 1993

**LIBRARY
Michigan State
University**

**PLACE IN RETURN BOX to remove this checkout from your record.
TO AVOID FINES return on or before date due.**

DATE DUE	DATE DUE	DATE DUE
01/19/2008	_____	_____
_____	_____	_____
_____	_____	_____
_____	_____	_____
_____	_____	_____
_____	_____	_____
_____	_____	_____

MSU Is An Affirmative Action/Equal Opportunity Institution

c:\circ\dstduea.pm3-p.]

**HIGH RESOLUTION ELECTRON MICROSCOPY
EXAMINATION OF DISLOCATION CORE
STRUCTURES IN B2 Ni-Al ALLOYS**

By

Scott Christopher Tonn

A THESIS

**Submitted to
Michigan State University
in partial fulfillment of the requirements
for the degree of**

MASTER OF SCIENCE

Material Science and Mechanics Department

1993

ABSTRACT

HIGH RESOLUTION ELECTRON MICROSCOPY EXAMINATION OF DISLOCATION CORE STRUCTURES IN B2 Ni-Al ALLOYS

By

Scott Christopher Tonn

[101] oriented single crystals with atomic percent compositions of Ni-48Al, Ni-50Al, Ni-51Al and Ni-52Al were deformed in compression at 400° C. Deformation properties have been characterised by optical slip trace and diffraction contrast analyses. Stoichiometric Ni-50Al exhibited a predominance of $\langle 001 \rangle \{100\}$ slip with some $\langle 001 \rangle \{110\}$ slip. The off-stoichiometric compositions displayed mostly $\langle 001 \rangle \{100\}$ slip with limited $\langle 001 \rangle \{110\}$ slip. High resolution electron microscopy was used to directly examine the $\langle 001 \rangle \{100\}$ edge dislocation cores to reveal the differences in core structure between the different compositions. The differences in mechanical properties between these compositions have been rationalized from these observations. The experimental core images have been compared to theoretical core images based on the embedded atom method. The theoretical models have been found to accurately predict the core structure in the stoichiometric alloy but only partially predicts the off-stoichiometric core structure properties.

DEDICATION

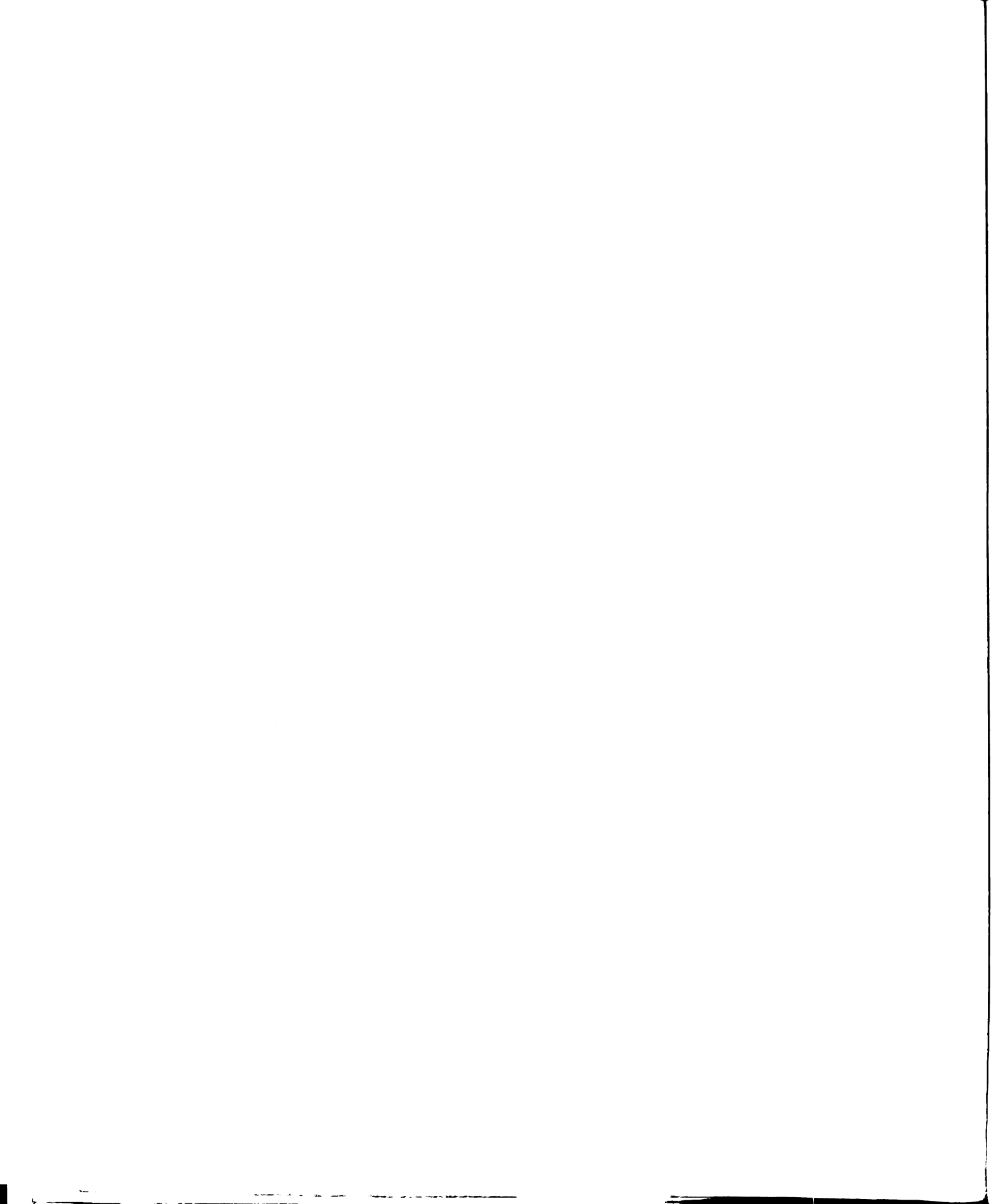
**To my Mother and Father,
for all of their help and support throughout the
pursuit of my goals.**

ACKNOWLEDGEMENTS

I would like to acknowledge and thank the office of Naval Research for the funding and support of this project under contract number N00014-90-J-1910. I would also like to acknowledge the following groups and people for their technical support and help. Dr. Ram Darolia at General Electric Aircraft Engine Division, for the supply of Ni-Al single crystal material. Mr. R. Mahapatra at the Naval Air Development Center, for single crystal material. Dr. John Mansfield at the University of Michigan Electron Microbeam Analysis Laboratory, for the use of the high resolution microscope. Dr. D. Farkas and Mr. Z. Xie of Virginia Polytechnic Institute and State University, for providing the results of their EAM calculations. Dr. D. S. Grummon, for the use of his lab equipment and the help of his assistants. I would like to thank the individuals whom helped me in one way or another to get through my thesis work. Suj, for his graciousness in letting me use his computer and his ever endearing moral support. Dr. Martin Crimp, for all his assistance as my advisor in helping me understand the concepts of this project, and for his support. Mr. Yu Zhang, for all his kindness and infinite support throughout this project. And finally, Megan, for all her support, love, and encouragement to get through the toughest of times throughout this project, and our lives.

Table of Contents

List of Tables.....	iv
List of Figures.....	v
1. Introduction.....	1
1.1 Background.....	2
1.2 Mechanical Properties.....	7
1.3 Dislocation Core Structure in bcc.....	15
1.4 Dislocation Core Structure in B2.....	15
1.5 Dislocations Observed in Ni-Al.....	22
1.6 Objective.....	23
2. Procedure.....	24
2.1 Compression Sample Preparation.....	24
2.2 Compression Testing.....	29
2.3 Optical Slip Trace Analysis.....	29
2.4 TEM Observation.....	30
2.5 Computer Simulation.....	31
3. Experimental Results.....	32
3.1 Slip Trace Analysis.....	32
3.2 Dislocation Substructure.....	32
3.3 $\mathbf{g} \cdot \mathbf{b} = 0$ Analysis.....	34
3.4 HREM Observation.....	41
4. Discussion.....	52
4.1 Mechanical Properties.....	52
4.2 Dislocation Core Spread.....	53
4.3 Computer Simulation of HREM.....	60
4.4 Dislocation Core Structure.....	63
5. Conclusions.....	75
6. References.....	77



List of Tables

<u>Table</u>	<u>Page</u>
1. List of nominal compositions of single crystal used in this investigation with respective source. GE and NADC are abbreviations for General Electric and Naval Air Development Center respectively. *This composition does not appear in the results of this investigation.....	25

List of Figures

<u>Figure</u>	<u>Page</u>
1. Plot of thermal conductivity for Ni-50Al in comparison to a typical Ni-based superalloy as a function of temperature. Adapted from [1].....	3
2. Phase Diagram illustrating the atomic structure as a function temperature for the Ni-Al alloy system. Adapted from [9].....	4
3. Several of the various AB and AB ₃ structures found in ordered intermetallic alloys.....	6
4. Plot of plastic strain at point of failure for <100> and <110> single crystal NiAl deformed in tension as a function of temperature. Adapted from [8].....	8
5. Plot of .2% yield stress as a function of temperature for various orientations and deformation schedules of Ni-Al in comparison to the traditional superalloy Rene 80. Adapted from [1].....	9
6. Plot of single crystal hardness as a function of stoichiometry at 200 ^o C for FeAl, NiAl and CoAl. Adapted from [16].....	11
7. Plot of creep strain rate vs. uniaxial stress for NiAl and CoAl at 1100 ^o C. Adated from [12].....	12
8. Plot of diffusion coefficient (D) as a function 1/T for CoAl and NiAl. Adapted from [14].....	13
9. Bar plot illustrating the approximate creep strengths of several different intermetallic compounds in comparison to several different superalloys. Adapted from [17].....	14
10. (a) and (b), computer model of two possible <111> screw dislocations in bcc. Atomic positions and displacement differences for a screw dislocation with $b=1/2[111]$. (c) Orientation showing relaxaton planes for the model core structures. Adapted from [19].....	16

List of Figures (Cont.)

<u>Fig.</u>	<u>Page</u>
11. Schematic of two possible $b=\langle 111 \rangle$ dislocations in the B2 structure. Both configurations have a next neighbor antiphase boundary.....	17
12. Computer model of a $b=[111]$ screw dislocation in Ni-50Al. Atomic displacements are represented as vectors projected onto the (111). The line direction is [111]. Adapted from [28].....	19
13. Differential displacement map for a core structure of the $1/2\langle 110 \rangle$ edge dislocation. The APB is on the (001) plane. Adated from [29].....	20
14. Model showing the core structure of a screw and edge (a and b respectively) dislocation with a burgers vector of [-110] on the (110). Adapted from [28].....	21
15. Example Laue back reflection pattern from a Ni-50Al single crystal with a high index orientation. The high definition diffracted spots give a qualitative indication of the low amount of defects within the crystal.....	26
16. (a) Stereographic projection of the (101) oriented compression specimens. (b) Schematic of the top surface of a compression specimen with respect to the crystallographic orientation.....	27
17. Schematic showing direction and face perspectives of the single crystal compression specimen. The notch on the North-East face corner is to preserve the rotational symmetry.....	28
18. (a) Optical micrograph showing the north face of a deformed ($\epsilon_p=5\%$) single crystal of Ni-50Al. (b) Optical micrograph showing the slip traces on the east face of a deformed Ni-50Al single crystal.....	33
19. Diffraction contrast image with a foil normal of [001] and a diffracting vector of (110). This micrograph shows the basic dislocation substructure of Ni-50Al with the appropriate line directions.....	35

List of Figures (Cont.)

<u>Fig.</u>	<u>Page</u>
20.	(a) Diffraction contrast image showing an area with several different dislocations in good contrast labeled <i>a</i> and <i>b</i> . The diffracting vector is (110). (b) Schematic showing a simplified version of figure 20 (a). The various dislocations are labeled <i>a</i> and <i>b</i> to make the difference distinguishable. (c) Diffraction contrast image showing an area with dislocations labeled <i>b</i> in contrast and dislocations labeled <i>a</i> out of contrast. The diffracting vector is (020) near a {001} zone. (d) Diffraction contrast image showing dislocations <i>a</i> out of contrast while <i>b</i> are in contrast. The diffracting vector is (011) near a {110} zone. (e) Diffraction contrast image showing an area with dislocations labeled <i>a</i> in contrast and dislocations <i>b</i> out of contrast. The diffracting vector is (200) near a {100} zone. (f) Diffraction contrast image showing most of dislocations labeled <i>b</i> out of contrast while dislocations <i>a</i> are in contrast. The diffracting vector is (101) near a {110} zone.....
	36
21.	Schematic showing the slip systems activated during compression. The appropriate dislocations are labeled accordingly.....
	40
22.	Diffraction contrast micrograph with foil normal of [010]. The dark spots represent dislocations with an end on configuration for imaging in phase contrast conditions. The diffracting vector is (101).....
	42
23.	(a) Diffraction spot pattern of a single crystal thin foil of Ni-50Al, showing a {100} zone for the B2 crystal structure with no objective aperature. The additional diffraction spots are created from the superlattice. (b) The same {100} zone with an objective aperature to limit the number diffracted beams for phase contrast imaging.....
	43
24.	(a) Phase contrast image showing the point to point resolution of the regular lattice in Ni-48Al at 350kV accelerating voltage. (b) schematic showing the B2 structure and point to point displacements. The light circles represent Ni-atoms and the dark represent Al.....
	44

List of Figures (Cont.)

<u>Fig.</u>	<u>Page</u>
25. Phase contrast image of a Ni-50Al [100] (001) edge dislocation. The foil normal is [010]. The image was taken at an accelerating voltage of 350kV.....	45
26. Phase contrast image of a Ni-48Al [100] (001) edge dislocation. The foil normal is [010]. The image was taken with an accelerating voltage of 350kV.....	47
27. Phase contrast image of a Ni-52Al [100] (001) edge dislocation. The foil normal is [010]. The image was taken with an accelerating voltage of 350kV.....	49
28. Phase contrast image of a [-110] (110) edge dislocation in Ni-51Al. The burgers circuit is diagramed around the core to illustrate the displacement. The foil normal is [010]. The image was taken at an accelerating voltage of 350kV.....	51
29. Schematic of edge dislocation core showing atomic positions for relatively locally compressed configuration. The subsequent plots below the illustration detail the disregistry, Δu , of the regular lattice and the burger's vector distribution function, $f=d(\Delta u)/dx$	55
30. Schematic of an edge dislocation core showing atomic positions for a spread configuration. The subsequent plots below the illustration detail the disregistry, Δu of the regular lattice and the burger's vector distribution function, $f=d(\Delta u)/dx$	56
31. Digitized image of the Ni-50Al core structure originally pictured in figure 25. The core image has been elongated to better illustrate the displacement out of the slip plane.....	57
32. Digitized image of the Ni-48Al core structure originally pictured in figure 26. The core image has been elongated to better illustrate the displacement out of the slip plane.....	58
33. HREM simulations showing the effect of thickness changes. The defocus is 60 nm. The thickness values are (a) 2.871 nm, (b) 5.741 nm, (c) 8.613 nm, (d) 11.484 nm.....	61
34. HREM simulation showing the effect of defocus. The foil thickness is 7.71 nm. The defocus values are (a) 40 nm, (b) 45 nm, (c) 55 nm, and (d) 60 nm.....	62

List of Figures (Cont.)

<u>Fig.</u>	<u>Page</u>
35. Projected potentials for two possible $\langle 100 \rangle \{001\}$ edge dislocations for Ni-50Al. (a) 'symmetric', (b) 'asymmetric' [28]	64
36. Illustration of the EAM dislocation core models, (a) details the effects of the 'symmetric' core structure and (b) represents the 'asymmetric' core structure. The difference between the two cores is the termination atom of the two extra half planes. The light circles represent Al atoms and the dark circles represent the Ni atoms.....	65
37. Atomic position maps based on EAM calculations for Ni-50Al, (a), and for local substitutions of an Al vacancy (c). (b) and (d) are HREM simulations for (a) and (c) respectively. Atomic position maps based on EAM calculations for a Ni vacancy (e), and for local substitution of an extra Al atom (g). (f) and (h) are HREM simulations of (a) and (g) respectively. Atomic position maps based on EAM calculations for extra Ni atom, (i), and for a local switch of an Al with Ni atom (k). (j) and (l) are HREM simulations of (i) and (k) respectively.....	67
38. Phase contrast image of a Ni-50Al $[100] (001)$ edge dislocation. The foil normal is $[010]$. The image was taken at 350 kV accelerating voltage. The arrows indicate the apparent extra two half planes along the $\{110\}$ planes.....	70
39. Schematic representation of the dislocation pictured in figure 28. The half plane termination planes are labeled as 'a' and 'b' and the termination atoms are represented as black circles.....	71
40. Phase contrast image of an apparent $b=1/2[110]$ edge dislocation in Ni-51Al. This image was taken at an accelerating voltage of 350 kV.....	73

1. Introduction

The B2 intermetallic aluminides have gained increased attention for their possible application in corrosive high temperature aircraft engine environments [1]. They are high melting point temperature materials that exhibit good oxidation resistance due to their large fraction of aluminum. In addition to their oxidation resistance and high melting points, they have relatively lower densities than traditionally employed superalloys. However, these B2 compounds lack appreciable ambient temperature ductility and toughness. The room temperature properties of these alloys makes mechanical forming difficult and cost ineffective, as well as limit the possible applications of these materials. The inability of this class of alloys to withstand low temperature damage, coupled with the expense of mechanical forming, discourages the commercial development of the B2 aluminides. Inherently low cleavage stresses [2] or the inability to initiate significant plastic flow through the activation of dislocation slip [3-5] may explain the inability of these materials to demonstrate adequate room temperature toughness. A better understanding of the mechanisms which govern the initiation of plastic deformation and the slip of dislocations in these compounds could better explain the observed properties. Increased knowledge of the core structure of dislocations found in these materials, specifically Ni-Al, may provide a basis for the promotion of the development of the intermetallic aluminides. These attractive qualities of this class of materials have initiated several research investigations to gain a better understanding of their properties [6,7]. Increased knowledge of the dislocation core structure through experimental observation may provide a better basic understanding of these materials in general as well as promote their commercial development.

The motivation for interest in the ordered intermetallics stems from the potential weight savings gained in employment of these materials as a replacement to the existing superalloys in use. A typical Ni-based super alloy has a density of 6 to 7 g/cc, whereas Ni-Al has density of 5.85 g/cc . This net weight savings would be on the order

of 5-10%. However, the effective overall weight savings could be as high as 40-50% when the rotational motion of these components in turbine engine applications is taken into consideration. The reduction in weight of these engine components would decrease the centrifugal force and thus reduce the weight needed to house the internal engine, effectively reducing the entire aircraft weight and inevitably increasing the aircraft efficiency.

In addition to the attractive weight savings, Ni-Al has a higher thermal conductivity than most Ni-based super alloys. Figure 1 shows the variation of thermal conductivity for Ni-Al in comparison to a Ni-based superalloy for a range of temperatures [1]. At any given temperature, the thermal conductivity of Ni-Al is substantially higher than that of the Ni-based super alloy. The significance of higher thermally conducting engine components is reflected in the need for the "hot spot" section of the turbine engine blade to be exposed to relatively high temperatures. A material that dissipates the heat away from the engine blade would allow the engine to operate at significantly higher temperatures, thus increasing the aircraft's efficiency. This increased thermal conductivity of Ni-Al also adds to the attractive properties for use in higher temperature aircraft environments.

The potential weight savings and thermal benefits of using Ni-Al as a high temperature corrosive environment material are evident. However, before commercial development of Ni-Al as a contender in the aircraft engine market can begin, more is needed to be known about this material and of ordered intermetallics in general.

1.1 Background

Typically an intermetallic compound is one that occurs over a narrow range of the phase diagram of a metal-metal system. Although these intermetallic compounds are usually restricted to definite stoichiometries, there are some compounds that exist over a range of compositions and are not strictly bound by a single composition (fig. 2) [8]. The intermetallic phases are found in single phase fields such as γ and β . The

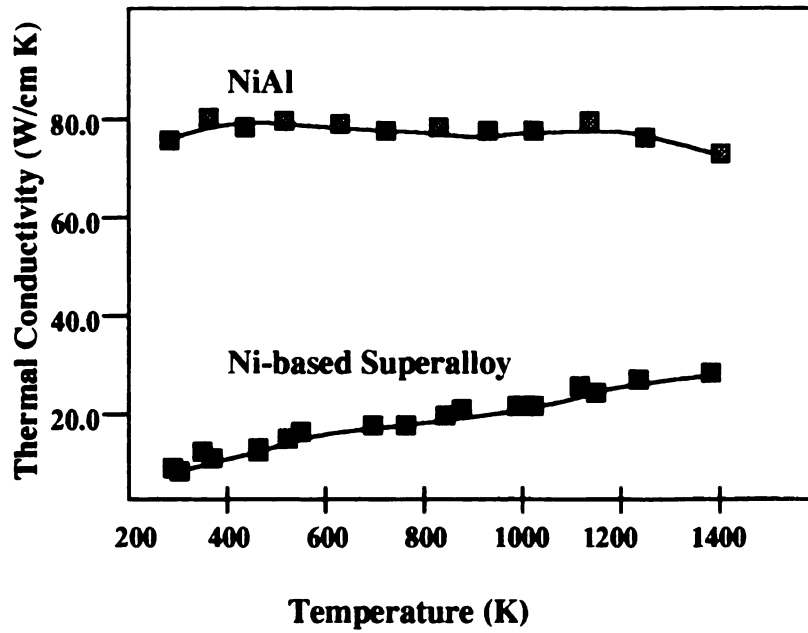


Figure 1 : Plot of thermal conductivity for Ni-50Al in comparison to a typical Ni-based superalloy as a function of temperature. Adapted from [1].

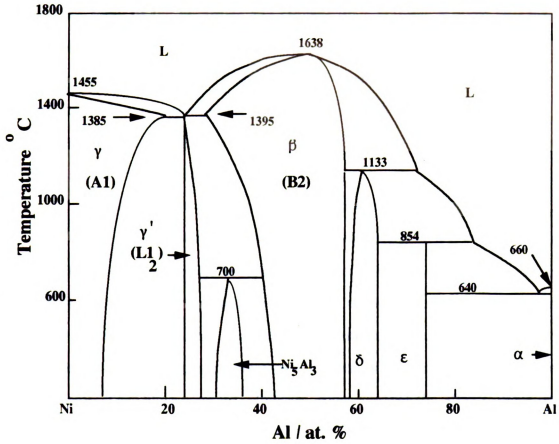


Figure 2: Phase diagram illustrating the atomic structure as a function of temperature for the Ni-Al alloy system. Adapted from [8].

intermetallic type of bonding can be described as bonding that is primarily metallic, but possesses some of the properties and characteristics inherent of ionic or covalently bonded systems [7]. Although intermetallics possess many of the typical metallically bonded systems qualities like high values of thermal and electrical conductivity, they exhibit covalent or ionic like properties such as high strength and stiffness. The hardness and yield strength is considerably higher than that of the binary constituents, as revealed in earlier investigations [6, 7].

Thermodynamic consideration of the nature of bonding in typical AB, AB₂, and AB₃ (fig. 3) compounds reveals that based on bond energies, it is energetically more stable for the A-B type bonds to form than A-A or B-B. This A-B bonding, or unlike nearest neighbor bonding, results in ordering. Ordering is common in intermetallic alloys and is found to be a function of temperature in most systems (i.e. order decreases with increasing temperature) as in the case of beta brass which loses its order well below its melting point [9]. However, some intermetallic alloy systems remain ordered up to their melting point, such as Ni-Al, Fe-Al and Co-Al systems [8].

Ni-Al, Fe-Al and Co-Al share similar qualities in many respects. The densities of these materials differ by a couple percent (5.85, 6.08, and 5.56 g/cc, respectively). All three alloys at the stoichiometric composition (50 at.% Al) have the B2 ordered structure with Ni-Al and Co-Al having similar congruent melting point temperatures (1913K and 1921K respectively). All three alloy systems exhibit the B2 order with solubilities ranges around the stoichiometric composition. The melting point temperatures of these alloy systems are all relatively high ($1300^{\circ}\text{C} < T_m < 1680^{\circ}\text{C}$) [10] and are comparable to one another. Yet, there are basic significant differences in the observed properties of these materials that are not explained by argument of structure and composition.

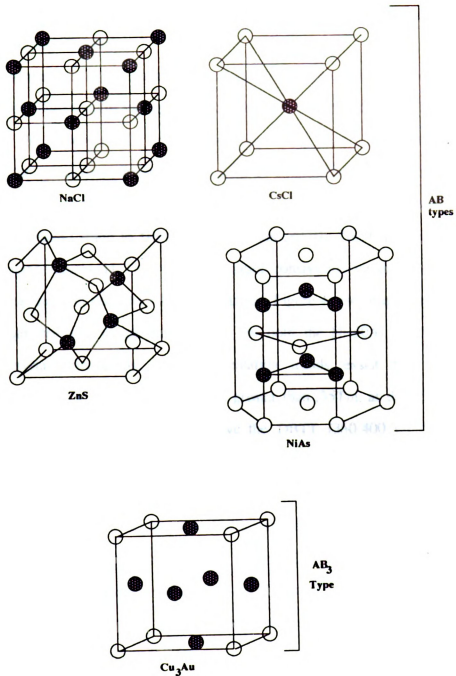


Figure 3: Several of the various AB and AB₃ structures found in ordered intermetallic alloys.

1.2 Mechanical Properties

Almost all of the ordered intermetallics display a large degree of elastic anisotropy. The modulus values for Ni-50Al are 94.46 GPa, 184.51 GPa and 270.43 GPa for the $\langle 100 \rangle$, $\langle 110 \rangle$ and $\langle 111 \rangle$ compression axes respectively [11]. These moduli and yield strengths are also sensitive to temperature. The plastic strain at the point of failure also exhibits a strong orientation dependence in single crystals. Figure 4 shows the plastic strain to failure of $\langle 100 \rangle$ and $\langle 110 \rangle$ Ni-50Al single crystals at various temperatures [1]. The $\langle 110 \rangle$ orientation consistently yields more plastic strain before fracture than does the $\langle 100 \rangle$ orientation. Figure 4 also illustrates the ductile to brittle transformation temperature (DBTT) for both the Ni-50Al $\langle 100 \rangle$ and $\langle 110 \rangle$ single crystal orientations. Similar orientation trends exist for most of the intermetallics, with many having DBTT's greater than $.35T_m$, as does the $\langle 100 \rangle$ Ni-50Al. Deformations performed just above the DBTT (350-400 C) [12] exhibit a substantial amount more plastic strain, as shown in figure 4. Thermally assisted processes are suspected to be activated at these temperatures. These processes could include dislocation climb, freeing of dislocations from impurities and possible deviations in the degree of order in the system [13]. It is not entirely clear what mechanisms are involved in the increase in ductility in this temperature range.

Previous studies of the various ordered intermetallic systems have demonstrated limited usefulness. However, it is important to recognize that the various phases of the intermetallic aluminides have long been utilized as reinforcing second phases in superalloys, such as γ' -Ni₃Al in most Ni-based superalloys. Although intermetallics in general have received considerable attention, the ordered intermetallic aluminides (i.e. Ni, Co, Fe) have received a large fraction of this attention recently [14, 15], particularly the Ni-Al system. Figure 5 shows .2% yield stress for several orientations of single crystal Ni-50Al in comparison with a traditional commercial super alloy as a function

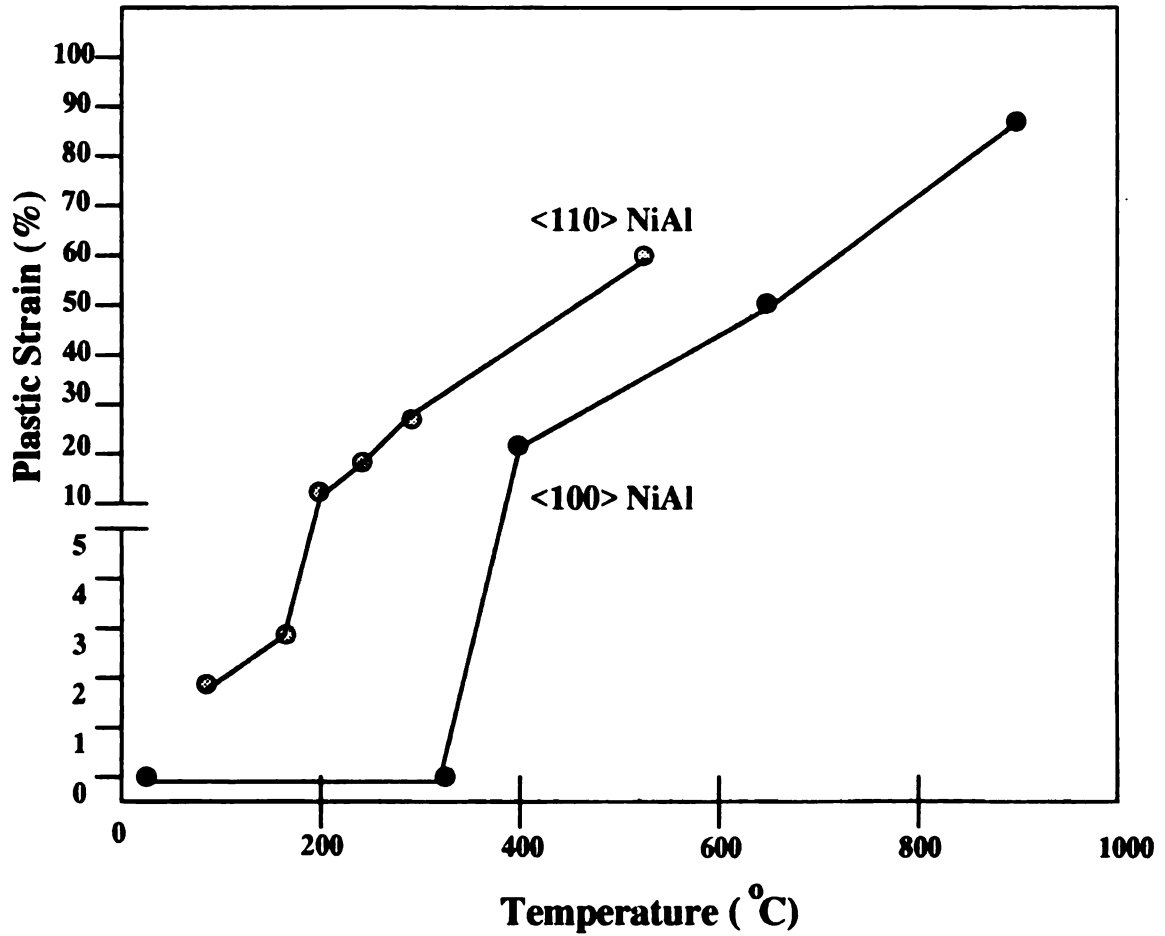


Figure 4: Plot of plastic strain at point of failure for <100> and <110> single crystal NiAl deformed in tension as a function of temperature. Adapted from [1].

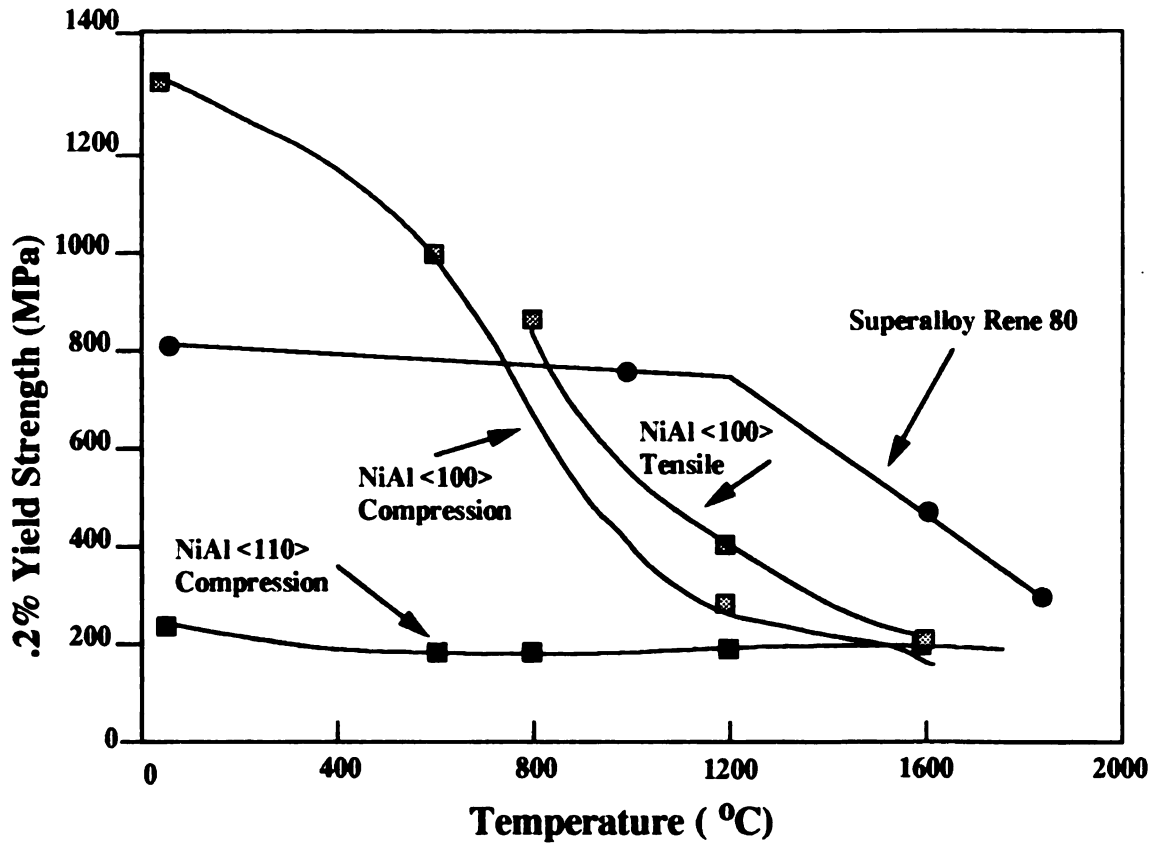


Figure 5: Plot of .2% yield stress as a function of temperature for various orientations and deformation schedules of Ni-50Al in comparison to the traditional superalloy Rene 80. Adapted from [1].

of temperature [1]. For most orientations of intermetallic Ni-50Al, the .2% yield stress of a standard superalloy is more reasonable than various orientations of Ni-50Al. This is further indication that Ni-Al is not as mechanically attractive. Further comparison of Ni-50Al to other ordered intermetallics displays differences between the similar intermetallics as well. Figure 6 displays Ni-Al, Co-Al, and Fe-Al single crystal hardness as a function of stoichiometry at a given temperature [16]. All three alloys depicted in figure 6 have very similar qualities with respect to structure, density, etc. However, the hardness of the Co-Al is consistently higher than Ni-Al or Fe-Al. Moreover, Ni-Al and Co-Al display increasing hardnesses away from the stoichiometric composition whereas Fe-Al does not. This increasing hardness phenomena in Co-Al and Ni-Al, and lack thereof in Fe-Al, suggests that the possibility of different active dislocations in the various aluminides.

The creep properties of Ni-Al and Co-Al differ greatly at high temperatures ($>1000^{\circ}\text{C}$) and stress levels (fig. 7 and 9) [14, 15]. However, the mechanisms by which they creep are the same. Both Co-Al and Ni-Al creep through dislocation creep [14]. The self diffusion rates for Ni and Co in Ni-Al and Co-Al are not much different than in the respective substituent metals [17]. The Ni-Al creeps at 1 to 2 orders of magnitude faster than does Co-Al at similar temperatures [14]. This suggests that there may be some difference in dislocation creep behavior, which may be influenced by the dislocation core structure. Thus, the dislocation core structure in Ni-Al may allow the material to creep at a higher rate. Again, neither Ni-Al or Co-Al have creep strengths that compare to commercial alloy that is currently utilized in high temperature environments. Figure 9 shows the various intermetallic aluminides creep strength at a given temperature in comparison to a commercial superalloy [15]. It can be seen that the intermetallic aluminides creep performance is substantially less than that of a commercial superalloy.

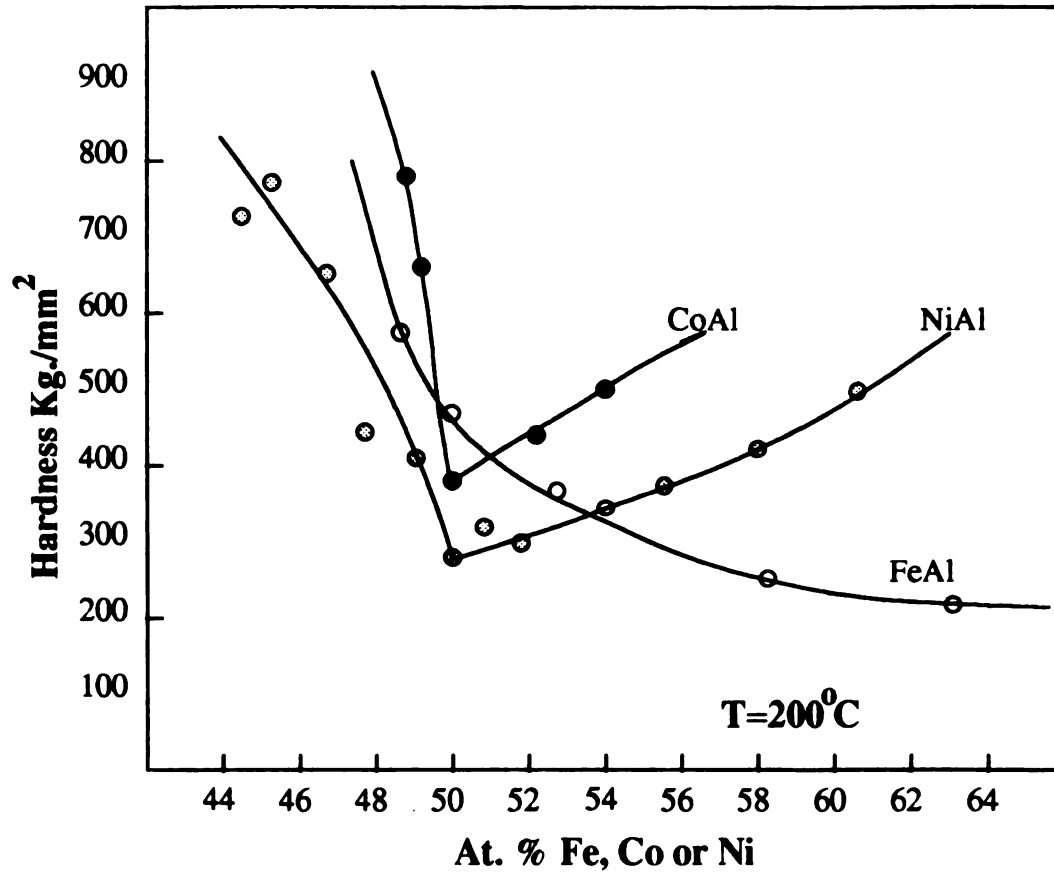


Figure 6: Plot of single crystal hardness as a function of stoichiometry at 200 C for FeAl, NiAl and CoAl. Adapted from [16].

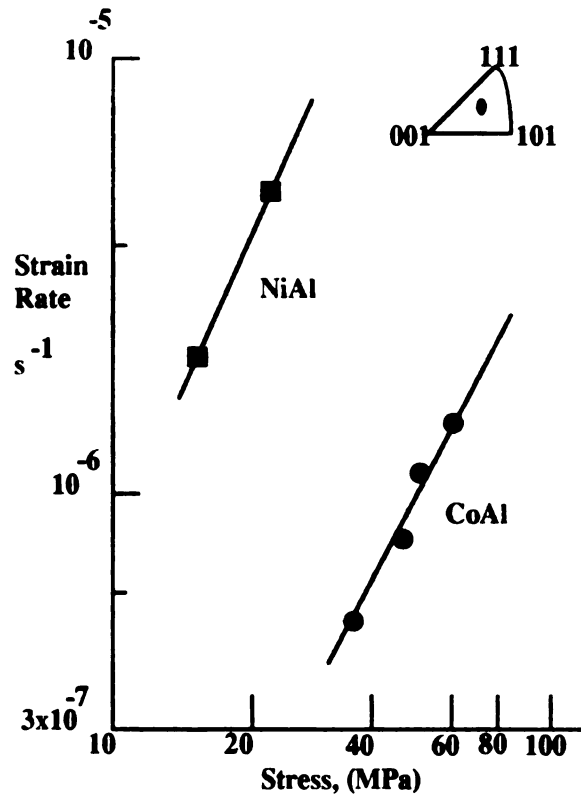


Figure 7: Plot of creep strain rate vs. uniaxial stress for Ni-50Al and Co-50Al at 1100 C. Adapted from [14].

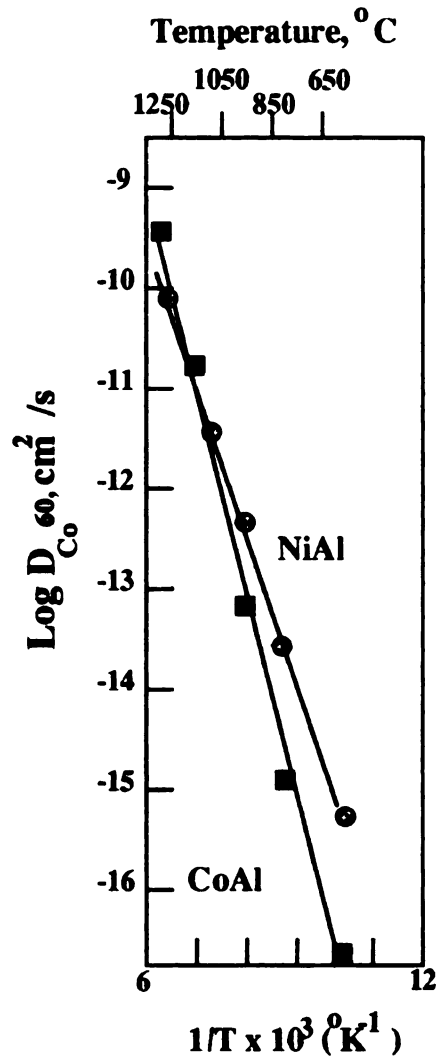


Figure 8: Plot of diffusion coefficient (D) as a function of $1/T$ for CoAl and NiAl. Adapted from [17].
 (Note: These two curves represent self diffusivities for the two alloys respectively.)

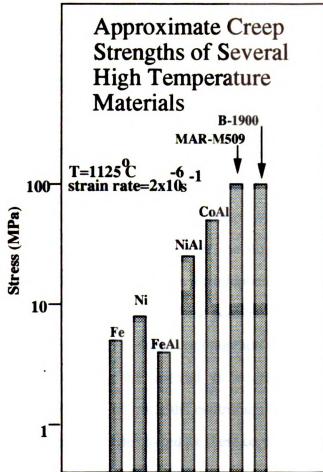


Figure 9: Bar plot illustrating the approximate creep strengths of several different intermetallic compounds in comparison to several different superalloys. Adapted from [15].

1.3 Dislocation Core Structures in bcc

It has long been known that $b=1/2\langle 111 \rangle$ screw dislocations control the mechanical behavior of bcc type materials. The core structure of these screw dislocations dictates the motion of these dislocations, and thus the observed mechanical properties [18]. Computer models have demonstrated that these screw dislocation have a three fold symmetry when relaxed. This three fold symmetry results in a non-planar core geometry [19-22]. Figure 10 (a and b) shows two possibilities of a $1/2[111]$ three fold symmetry screw dislocations with respect to crystallographic plane perspective (c) [19]. The atomic displacement map is superimposed on the supercell containing the dislocation core simulation. The displacement map uses the convention of vectors or arrows to represent the $[111]$ component of the displacement between two atoms projected on to the (111) plane centered on the midpoint of the two atoms. Figure 10 (c) exhibits the respective planes on which these possible displacements occur. The non-planar core must be reduced to a planar configuration for the dislocations to move on any given slip plane, enabling the material to be deformed plastically. The critical resolved shear stress (CRSS), which is the controlling factor in plastic deformation, is directly related to this stress needed to reduce these cores to a planar form.

1.4 Dislocation Core Structure in B2

The theoretical structure of the dislocations found in B2 materials have been investigated using pair potential models [23-27]. The core structure of the $1/2\langle 111 \rangle$ super partial screw dislocation in the B2 structure was found to be similar to the three fold relaxation found in bcc type materials. To preserve the long range order, the overall dislocation structure is made up of two $1/2\langle 111 \rangle$ dislocations separated by an antiphase boundary (APB) [23-25]. Figure 11 is an illustration of possible dislocation-APB configurations including two super partial dislocation separated by a nearest neighbor APB and an ordinary dislocation with an attached nearest neighbor APB. The slip planes that these dislocations move is the subject of some disagreement. Higher

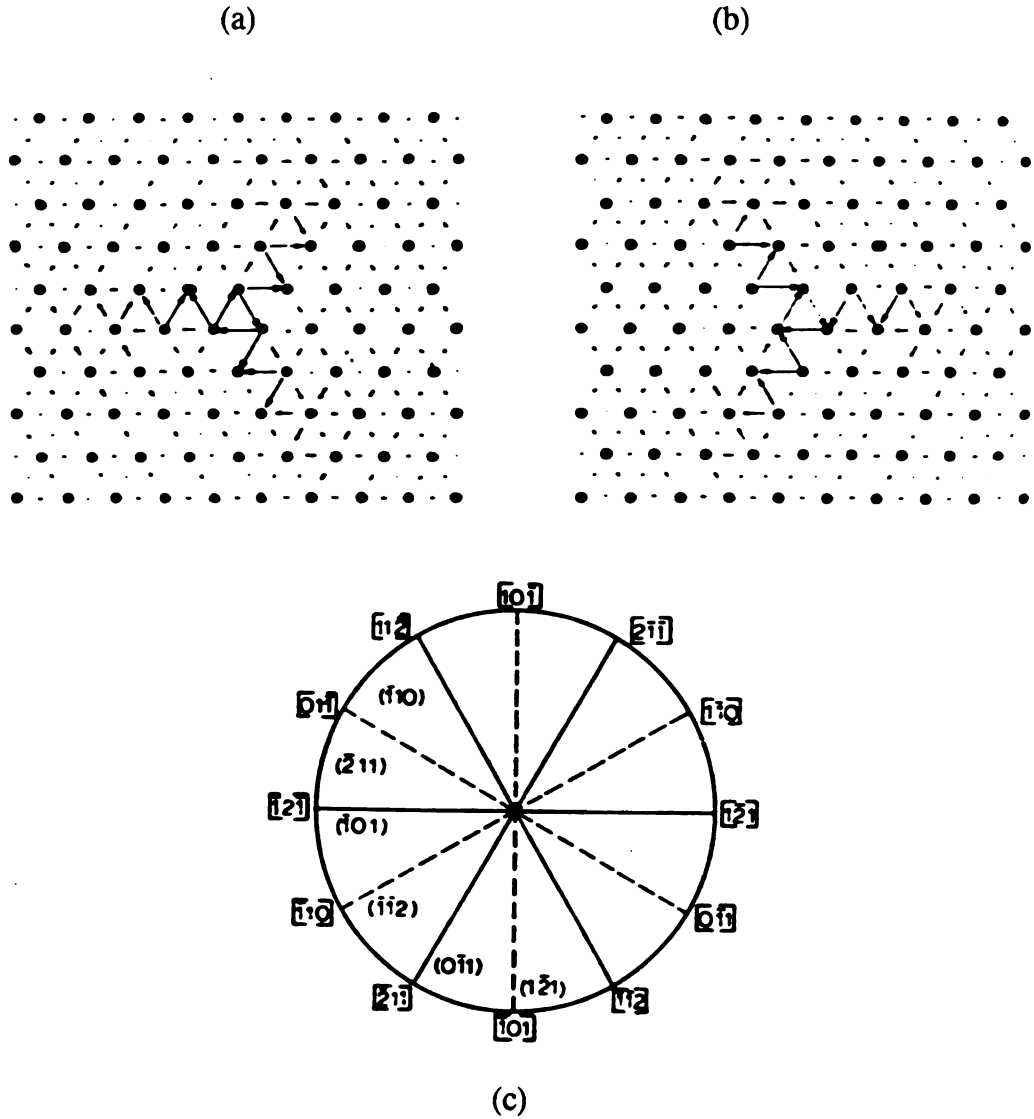


Figure 10: (a) and (b) Computer model of two possible $\langle 111 \rangle$ screw dislocations in bcc. Atomic positions and displacement differences for a screw dislocation with $b=1/2[111]$. (c) Orientation showing relaxation planes for the model core structures. Adapted from [19].

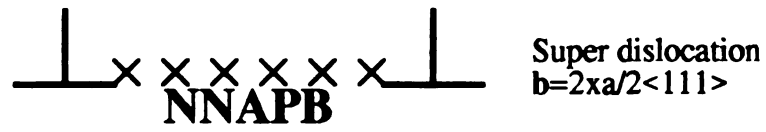
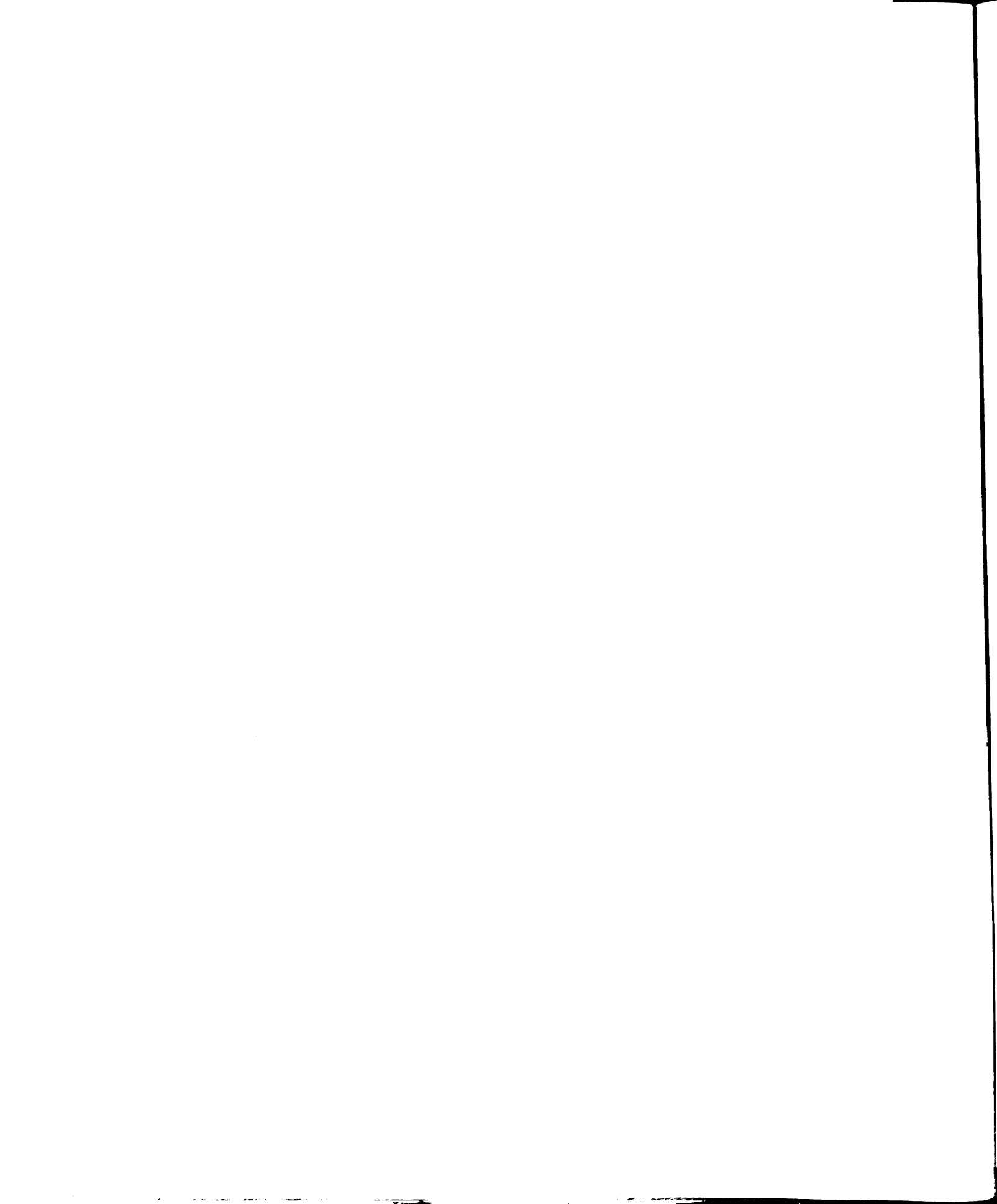


Figure 11: Schematic of two possible $b=\langle 111 \rangle$ dislocations in the B2 structure. Both configurations have a next neighbor antiphase boundary.



APB energy $\langle 111 \rangle$ dislocations have been calculated to slip on $\{110\}$ planes whereas lower APB energy $\langle 111 \rangle$ dislocations have been theorized to slip on $\{112\}$ planes [23]. However, $\{112\}$ or $\{110\}$ slip planes have been observed experimentally regardless of the APB energy [26]. As it appears, the complex interactions between the dislocation core and the APB energy are not completely understood. Figure 12 shows a computer model of one of these $[111]$ screw dislocations comprised of two superpartials on the (110) plane with the cores of the superpartials relaxing on the $\{112\}$ planes [28].

Studies on $\langle 100 \rangle$ and $\langle 110 \rangle$ type dislocations in B2 materials are also found in the literature [24, 27]. Computer modelers have demonstrated that these screw dislocations relax in planar and non-planar fashion on $\{011\}$. Figure 13 shows one of these non-planar $1/2[1-10]$ screw dislocations with an APB on the (001) [29]. Figure 14 (a) and (b), exhibits a relaxed $[110]$ dislocation in both screw (non-planar) and edge (planar) configurations respectively. Hence, it is expected that slip of these planar dislocations should be more easily activated than slip of the $\langle 111 \rangle$ or $\langle 110 \rangle$ screw dislocations.

Many of these dislocation models do not take into account specific differences in bond energy and APB energy for the various specific B2 systems, such as Ni-Al vs. Fe-Al. These models are based on empirical pair potentials of a generic B2 system that are simply a difference in unlike nearest neighbor bonds being energetically lower than like nearest neighbor bonds [27]. These models however, may not predict actual alloy behavior. The reported mechanical properties of B2 alloys display significant differences between one another. Examples of this are Fe-Al, which exhibits slip with $\langle 111 \rangle$ dislocations at ambient temperatures [30, 31], whereas other systems such as Au-Zn display $\langle 100 \rangle$ slip at room temperature [31]. Individual system properties that are included in the model may make better predictions as to the core structure of the dislocations. For example Pasianot, et. al. [29] have used volume dependent pair

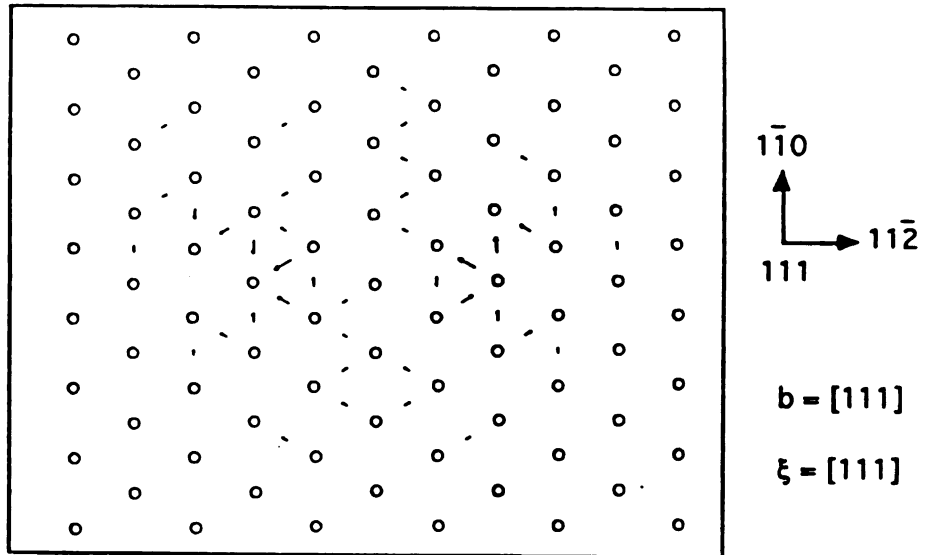


Figure 12: Computer model of a $b=[111]$ screw dislocation in Ni-50Al. Atomic displacements are represented as vectors projected onto the (111) . The line direction is $[1\bar{1}1]$. Adapted from [28].

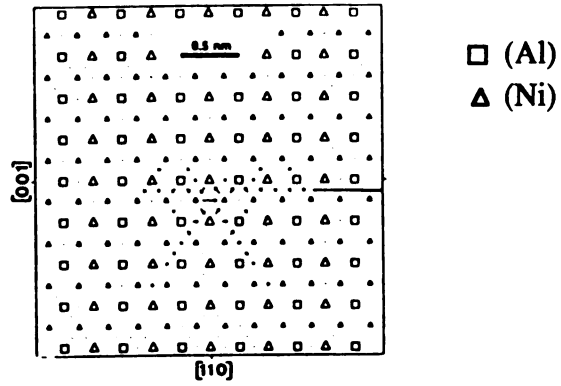


Figure 13: Differential displacement map for a core structure of the $1/2\langle 110 \rangle$ screw dislocation. The APB is on the (001) plane. Adapted from [29].

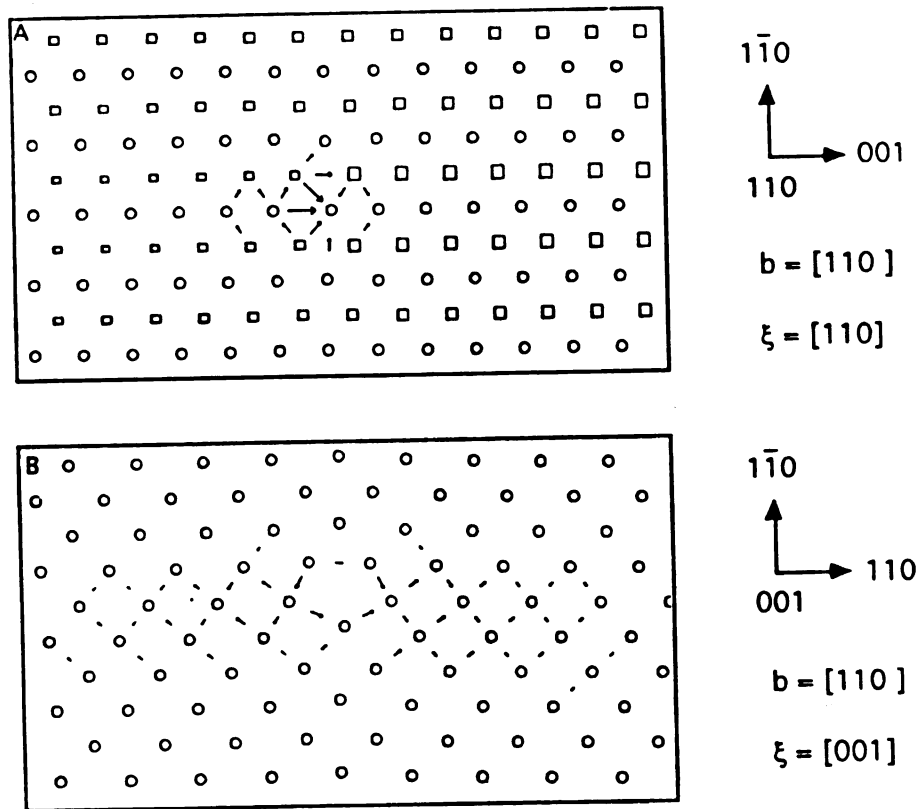


Figure 14: Model showing the core structure of a screw and edge(a and b respectively) dislocation with a Burgers vector of $[110]$ on the (110) . Adapted from [28].

potencia

with a

more a

1.5 D:

activa

majon

dislo

and

slip

<11

limi

ma

rea

sim

the

in

be

re

in

It

H

in

to

o

potentials to determine the structure of $\langle 111 \rangle$, $\langle 110 \rangle$ and $\langle 111 \rangle$ dislocations in Ni-Al with a variety of different slip planes and line directions. It is believed that these models more accurately predict the various specific system's dislocation core structures.

1.5 Dislocations observed in Ni-Al

Many studies may be found in the literature that have examined the slip systems activated in Ni-Al using slip trace analysis and electron microscopy [18, 32-35]. The majority of these findings have stated that the preferred slip system is $\langle 001 \rangle$ dislocations moving on $\{100\}$ or $\{110\}$ planes. These $\langle 001 \rangle$ dislocations on $\{110\}$ and $\{100\}$ planes have been found to exhibit both edge and screw character. $\langle 111 \rangle$ slip has also been reported in the literature [17, 36, 37]. Similar to bcc alloys, the $\langle 111 \rangle$ dislocations are observed as long straight screw dislocations with only limited edge components [36]. These $\langle 111 \rangle$ dislocations are not believed to be a major component of the plastic deformation properties of Ni-Al due to the inability to readily observe these dislocations with varying deformation schedules. $\langle 001 \rangle$ oriented single crystals deformed at relatively low temperatures have shown a greater number of these $\langle 111 \rangle$ screw dislocations. It is important to note that Von Mises's criterion of 5 independent slip systems is not met for slip in $\langle 100 \rangle$ Ni-Al. If sufficient slip were to be attained via $\langle 111 \rangle$ dislocations the criterion would be met and likely the ductile response would be observed. However, presently the dominant slip vectors observed in Ni-Al are $\langle 001 \rangle$.

Several studies have observed $\langle 110 \rangle$ dislocations in deformed Ni-Al [35, 38]. It is believed by some that these $\langle 110 \rangle$ dislocations slip independently [35, 38]. However, others [39] suggest that these $\langle 110 \rangle$ dislocations are formed through the interaction of $\langle 100 \rangle$ type dislocations ($\langle 100 \rangle + \langle 010 \rangle \rightarrow \langle 110 \rangle$) and do not contribute to the overall plastic deformation characteristics of Ni-Al. Recently, Miracle [40] has observed $\langle 110 \rangle$ dislocations in Ni-Al bi-crystals. Although Miracle states that the

overall

nuclea

1.6 Ot

crysta

consi

poss

the

diff

eva

lite

of

ob

hi

oi

overall mode of deformation is governed by $\langle 100 \rangle$ dislocations, he has observed the nucleation of $\langle 110 \rangle$ dislocation loops out of the bi-crystal interface.

1.6 Objective

Ni-Al and Co-Al are similar in many regards with respect to density and crystallographic structure. However, their respective mechanical behaviours vary considerably. This suggests that there may be differences in the dislocation motion, and possibly in the dislocation core structure between these two materials. Investigations of the dislocation core structure of these two materials may provide insight into the difference in mechanical properties of Ni-Al and Co-Al. There are many of studies evaluating the mechanical properties of the intermetallic aluminides found in the literature. However, there are very few detailed studies on the experimental observation of dislocation core structures in the various ordered aluminides [41, 42]. It is the objective of this study to directly examine the core structure of dislocations in Ni-Al via high resolution electron microscopy (HREM). Correlations to the differences in observed mechanical properties can then be made.

2. Experimental Procedure

2.1 Compression Sample Preparation

Various compositions of Ni-Al single crystals were obtained from General Electric Aircraft Engine division, Cincinnati OH, and by the Naval Air Development Center, Warminster PA. Table 1 lists the nominal stoichiometries and source of the single crystals used in this investigation. Not all of the compositions listed in table 1 appear in this investigation's results section. However, references to the composition accompany all reported results. The source of the material may be deduced by comparison to this table.

The bulk single crystals were oriented to a $\langle 011 \rangle$ by the Laue back reflection Xray technique. The quality of the diffraction pattern was an indication of the low amount of defects within the crystals (fig. 15). Gage length compression specimens were cut with a specific (101) orientation (figure 16 (a)) with the orthogonal faces of the rectangular specimen denoted as East, West, North and South for identification purposes (figure 16(b)). The specimens were sectioned such that there was an approximate 3:1 face width-to-length ratio to promote homogenous deformation throughout the specimen (figure 17). The $\langle 011 \rangle$ orientation was chosen to promote the activation of the $\{001\}$ slip planes. A notch was ground into one of the corners of the rectangular specimen to preserve the rotational orientation during sectioning. An Accutom 2 wafering saw with a Buehler Isocut diamond blade was used to section the material. The brittle nature of the material made handling of the material difficult. Caution was exercised in the sectioning operations, especially for the off-stoichiometry compositions.

The gage length specimens were ground with 600 grit SiC paper on all four faces. Once the faces of the specimen were sufficiently ground to an overall smooth appearance they were then hand polished with diamond paste. The polishing iterations started at 9 micron diamond slurry and dropped successively down to 3 micron, 1

Single Crystal Nominal Composition (at. %)	Source
Ni-52 Al	NADC
Ni-51Al	GE
Ni-50Al	NADC and GE
Ni-48.84Al	GE
Ni-48Al	NADC
Ni-45.87Al*	GE

Table 1: List of nominal compositions of single crystals used in this investigation with respective source. GE and NADC are abbreviations for General Electric and Naval Air Development Center respectively. *This composition does not appear in the results of this investigation.

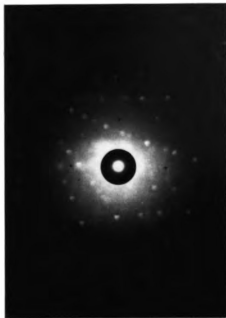


Figure 15: Example Laue back reflection pattern from a Ni-50Al single crystal with a high index orientation. The high definition diffracted spots give a qualitative indication of the low amount of defects within the crystal.

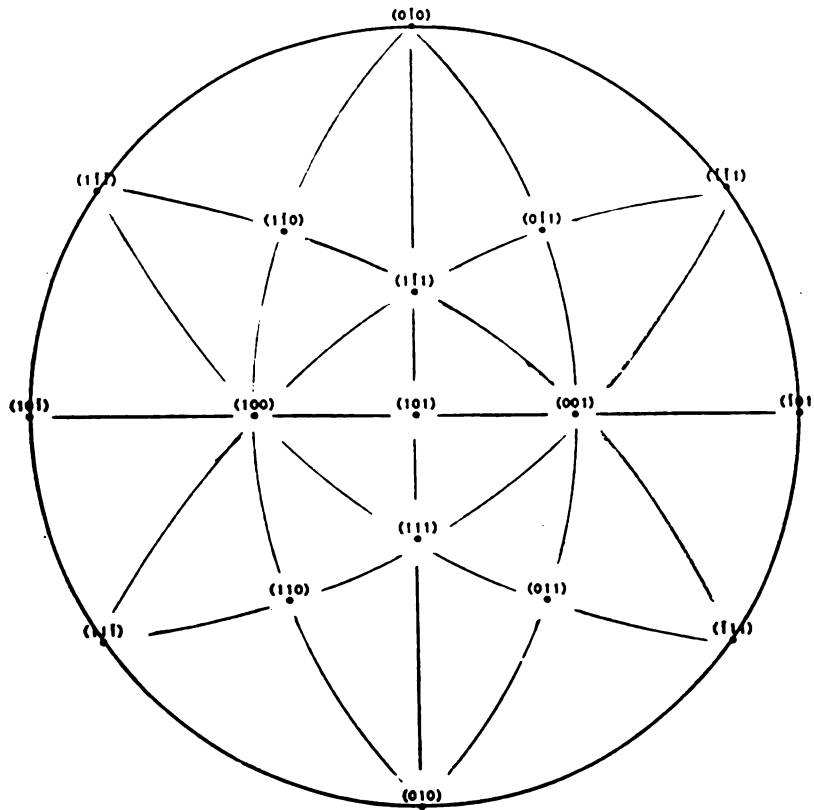


Figure 16(a): Stereographic projection of the (101) oriented compression specimens.

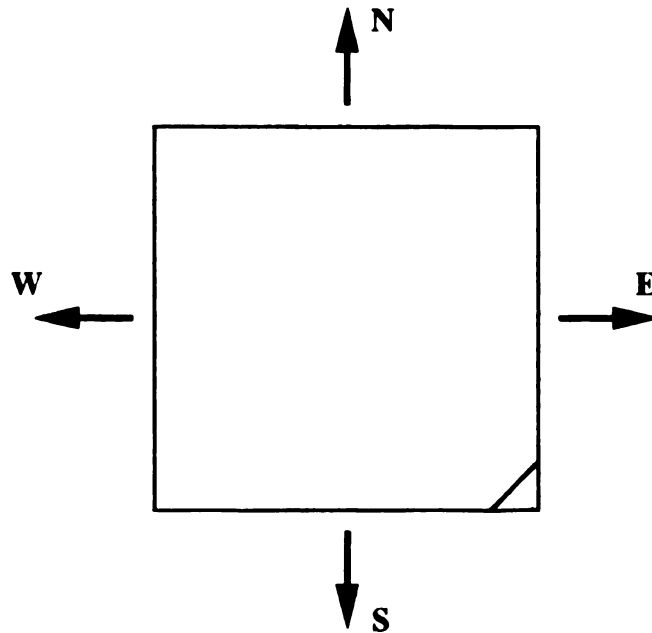


Figure 16(b): Schematic of the top surface of a compression specimen with respect to the crystallographic orientation.

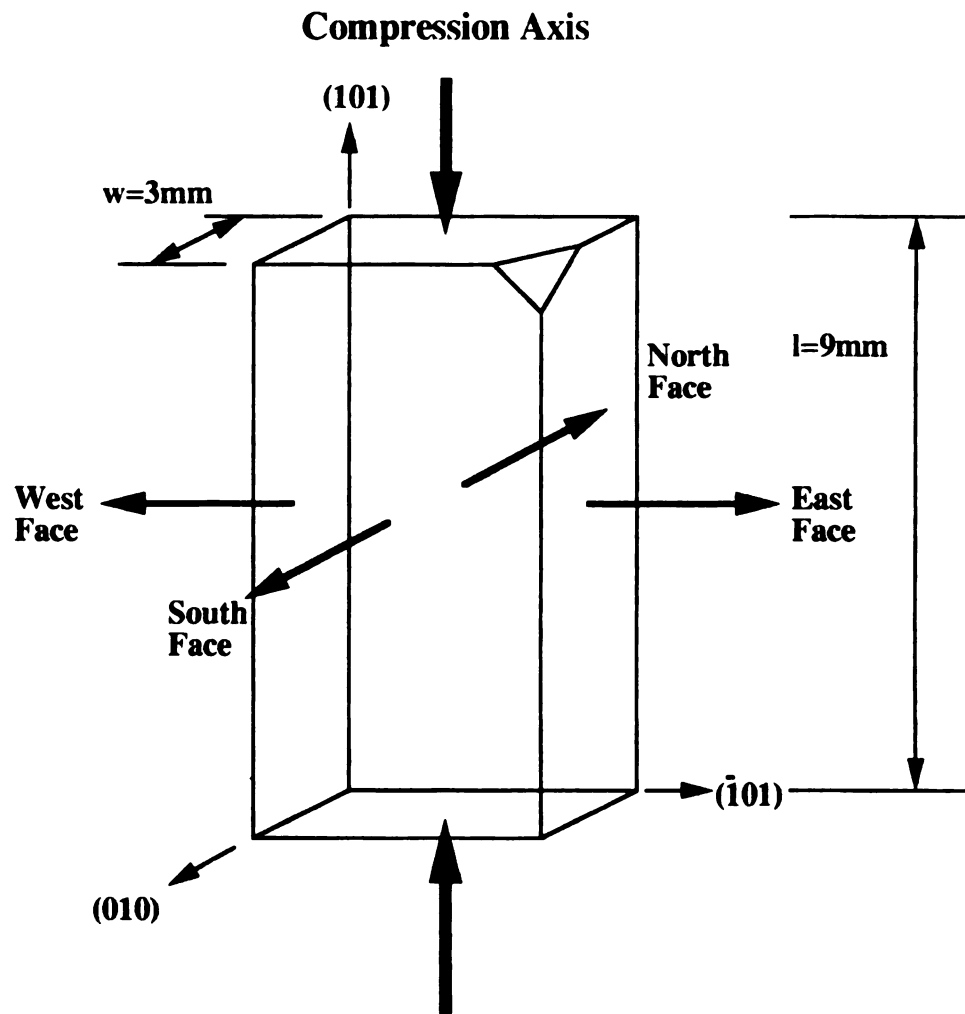


Figure 17: Schematic showing length and width dimensions and directional face perspectives of the single crystal compression specimen. The notch on the North-East face corner is to preserve the rotational symmetry.

micron, 0.5 micron, 0.1 micron. The polished specimens were then inspected visually to insure that no scratches or blemishes appeared on the faces of the specimen. The polish was performed on the specimen to make optical slip trace microscopy possible.

2.2 Compression Testing

The samples were deformed in compression on a MTS 810 axial loading test apparatus equipped with a Centorr vacuum furnace. The test temperature was set at 400° C. The temperature was chosen to insure a more ductile response of the material and that no other deformation processes such as creep occurred simultaneously. Furthermore, the 400° C temperature was chosen in an effort to duplicate a previous investigation's results [11] and to encourage $\langle 100 \rangle \{001\}$ slip. The compression was carried out at a strain rate of 10^{-4} s^{-1} to approximately $\epsilon_p=5\%$. The low value of plastic deformation allowed for significant plastic deformation without creating complex interactions of dislocations. The avoidance of these complex interactions was an attempt to make analysis of the dislocation substructure less difficult. The deformation was performed under a vacuum pressure of about 10^{-5} torr to inhibit oxidation of the material.

2.3 Optical Slip Trace

The slip trace analysis was performed using optical light microscopy. The slip lines were observed on the various faces of the specimen and the angles were measured with respect to the axial $\langle 011 \rangle$ direction. The measured angles were then transferred to the $\langle 011 \rangle$ stereographic projection which indicated the activated slip planes within the single crystal during compression. A more detailed description of the standard two face single crystal slip trace analysis may be found in the literature [43].

The deformed crystals were sectioned parallel to the slip plane with the diamond blade wafering saw. 3 mm discs were cut from the diamond blade sections using electro discharge machining (EDM). The cuttings were ground by hand to a thickness of no more than 0.15 mm using 600 grit SiC paper. The ground specimens were then electropolished/thinned in a Struers Tenupole twin jet polisher at -30 C under 12Volts

in a solution of 1 part nitric acid to 2 parts distilled methanol. The thin foils were prepared to perform the $g \cdot b = 0$ analysis to characterize the burgers vector and line direction of the dislocations present in the deformed specimen.

2.4 TEM observation

The $g \cdot b = 0$ analysis was performed on a Hitachi H-800 200kV transmission electron microscope under diffraction contrast conditions. The analyses were performed using the bright field imaging technique. The thin foils of the material were tilted to diffracting conditions of $g \cdot b = 0$ and $g \cdot b \times u = 0$ for the invisibility and near-invisibility criterion. Trace analysis of the bright field images with respect to the diffraction pattern revealed the line direction of the dislocations present in the crystal.

Once the line direction and character of the dislocations were determined, another set of similarly prepared $\langle 011 \rangle$ deformed single crystals were sectioned perpendicular to the line direction of the edge dislocation with a burger's vector of $\langle 100 \rangle$ on the $\{010\}$. The choice of $\langle 100 \rangle \{001\}$ dislocations was made due to the resolution limits of the 400kV microscope and the need to image via a low index zone. The projected interatomic spacing of the atoms on the cube plane is approximately 0.20nm, whereas the resolution limit of the microscope is approximately 0.17nm. The cube slip edge dislocations inhabit a low index zone ($\{010\}$) and have a low index line direction ($\{100\}$) which is also needed for phase contrast imaging.

The sections made perpendicular to the line direction of the edge dislocations were ground and electropolished/thinned in the same manner as the slip plane sections used for the $g \cdot b = 0$ analysis. The thin foils were then examined under phase contrast conditions in a JEOL 4000 EX 400kV TEM (operated at 350kV) equipped with Gatan video imaging system to directly image the atomic lattice. The HREM was performed at the University of Michigan Electron Microbeam Analysis Laboratory (EMAL).

The off-stoichiometric specimens were prepared similarly to the Ni-50Al. Due to the increased hardness of the Ni-52Al, and Ni-48Al, the cutting feed speeds of the

material were reduced. The slower feed speeds reduced the risk of fracture during the sectioning operation. The sample preparation techniques for the off-stoichiometric specimens, other than sectioning, were identical .

2.5 Computer Simulation

Computer simulation of HREM images were performed on a theoretical $\langle 100 \rangle$ $\{001\}$ model of the dislocation core structure using the EMS software package [44]. The EMS software accurately simulates the phase contrast imaging conditions on the computer model used in this investigation. The computer model supercells used in this investigation were supplied by Pasianot et. al. [29] and were made using the Embedded Atom Method (EAM). Comparison of the experimentally obtained phase contrast HREM images were made to the simulated HREM images of the core structure model. This computer simulation of the core structure model is nessecary to effectively evaluate the computer models accuracy in predicting the core structure of the $\langle 100 \rangle$ $\{001\}$ edge dislocations.

3. Experimental Results

3.1 Slip Trace Analysis

Optical slip trace analysis of the (101) oriented deformed ($T=400^{\circ}\text{C}$, $\epsilon_p=5\%$) stoichiometric Ni-50at%Al (here after denoted as Ni-50Al) revealed the activation of duplex {100} slip planes along with duplex {110} slip planes (fig. 18 (a) and (b)) (duplex slip is defined as the activation of both or all of a given {hkl} having the same slip plane normal angle with the compression axis). The samples were uniformly deformed displaying two distinctly different sets of slip lines corresponding to two of the {101} and the two {100}. The Schmid factors for the four {101} $\langle 010 \rangle$ and the two {100} $\langle 001 \rangle$ are .354 and .50 respectively. It was determined that there were four possible {110}, ((110), (1-10), (0-11), (011)) and two possible {100}, ((100), (001)) planes that would display the slip traces present on the various faces of the crystal (fig. 18 (a) and (b)). The observation of these activated duplex {100} and {110} slip planes is in good agreement with previous investigations found in the literature [11, 16]. Once the activated slip planes were determined, (001) parallel specimen sections were taken for TEM specimen preparation for the $g \cdot b = 0$ analysis.

After examining the optical slip line micrographs for the various compositions of Ni-Al (Ni-52Al, Ni-51Al, Ni-50Al, Ni-48Al), it became apparent that the Ni-50Al exhibited the activation of both duplex {110} and {100} with {110} being the dominant planes of slip. However, the off-stoichiometric compositions were dominated by the activation of {100} slip planes. Both the Ni-52Al and Ni-48Al compositions displayed {110} slip plane activation, but to lesser degrees than did the stoichiometric composition. This demonstrates that there is a shift in preferred dominant slip plane for compositions away from stoichiometry.

3.2 Dislocation Substructure

Ni-50Al TEM specimens sectioned parallel to (001) exhibited basically two general line directions of dislocations. The dislocations lying within the plane of the foil

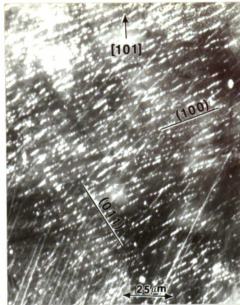


Figure 18 (a): Optical micrograph showing the north face of a deformed ($\epsilon_p = 5\%$) single crystal of Ni-50Al.

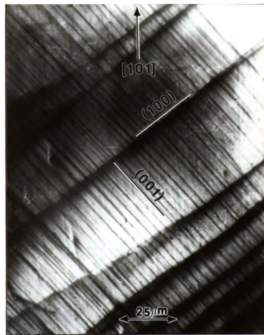


Figure 18 (b): Optical micrograph showing the slip traces on the east face of a deformed Ni-50Al single crystal.

were found to have line directions of $[100]$ and $[010]$ (fig. 19). In addition to the long straight dislocation segments, there were large concentrations of inclined dislocations lying in dense bands with an overall band direction of $[100]$. Since the long straight dislocations were lying within the plane of the foil, they were assigned to the (100) slip plane. The dense bands of inclined dislocations were presumably one of the possible $\{110\}$ slip planes. Figure 19 shows the general line directions for dislocations lying within and inclined to the plane of the (010) foil.

3.3 $\mathbf{g} \cdot \mathbf{b} = 0$ Analysis

Figure 20 (a) shows an area with two different sets of dislocations with different burgers vectors both in contrast. Figure 20 (b) shows a schematic of figure 20 (a) with dislocations labeled a and b accordingly. Figure 20 (c) and (d) shows dislocation type a out of contrast with diffracting vectors $\mathbf{g}=(020)$ and $\mathbf{g}=(011)$ respectively. By taking the cross product of these two diffracting vectors for which the invisibility criterion is met, dislocation type a is determined to have a burger's vector of $[100]$. Similarly, figure 20 (e) displays dislocation type b out of contrast for a diffracting vector of $\mathbf{g}=(200)$. However, it was not possible to find a diffracting vector such that all of the dislocations of type b were made to go out of contrast. This suggests that there may be more than one possible burger's vector for the dislocations inclined to the foil. Hence, the dislocations labeled b could not be diffitively assigned due to the difficulty to observe all of them out of contrast. However, the focus of this study was to study the $\langle 100 \rangle \{001\}$ dislocations. Figure 20 (f) shows some of the type b dislocations out of contrast for a diffracting vector of $\mathbf{g}=(101)$. Taking the cross product of these two diffracting vectors for the type b dislocation yields a possible burger's vector of $[010]$. However, close examination of the type b dislocations for the various diffracting vectors reveals that the invisibility criterion is not met for all of these dislocations. Hence, these type b dislocations can not conclusively be assigned as $\mathbf{b}=[010]$.

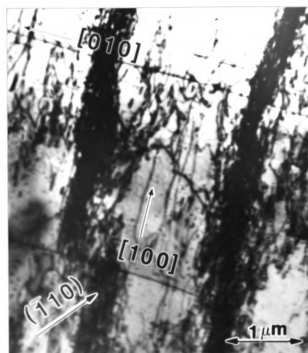


Figure 19: Diffraction contrast image with a foil normal of $[001]$ and a diffracting vector of (-110) . This micrograph shows the basic dislocation substructure of Ni-50Al with appropriate line directions.

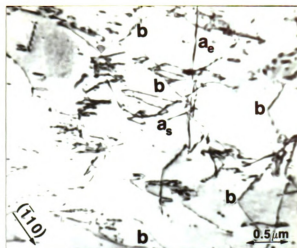


Figure 20 (a): Diffraction contrast image showing an area with several different dislocations in contrast labeled *a* and *b*. The diffracting vector is (-110) .

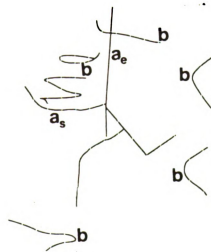


Figure 20 (b): Schematic showing a simplified version of figure 20 (a). The various dislocations are labeled *a* and *b* to make the difference distinguishable.

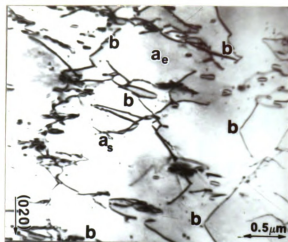


Figure 20 (c): Diffraction contrast image showing an area with dislocations labeled b in contrast and dislocations a out of contrast. The diffracting vector is (020) near a $\{001\}$ zone.

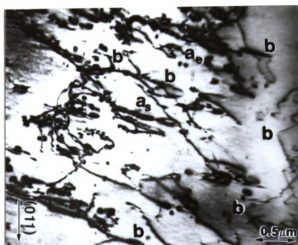


Figure 20 (d): Diffraction contrast image showing dislocations a out of contrast while dislocations b are in contrast. The diffracting vector is (011) near a $\{110\}$ zone.

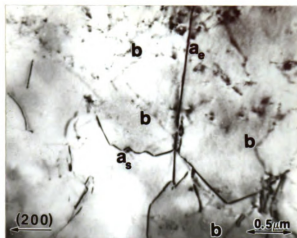


Figure 20 (e): Diffraction contrast image showing an area with dislocations labeled *a* in contrast and dislocations *b* out of contrast. The diffracting vector is (200) near a $\{001\}$ zone.

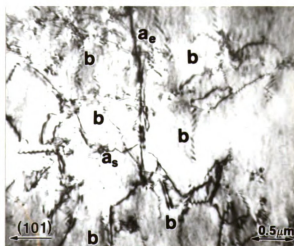


Figure 20 (f): Diffraction contrast image showing dislocations *b* out of contrast while dislocations *a* are in contrast. The diffracting vector is (101) near a $\{110\}$ zone.

The standard $g \cdot b = 0$ analysis and trace analysis revealed the type a dislocations with a line direction of $[010]$ to be pure edge on the (001) plane. The type a dislocations with a line direction of $[100]$ were found to be pure screw with a burger's vectors of $[100]$. In addition to these edge and screw dislocations, there were a substantial number of mixed dislocations with the $[001]$ burger's vector inhabiting the (001) plane. Figure 21 is a schematic displaying the findings of the $g \cdot b = 0$ analysis with respect to the slip trace analysis results showing the various activated slip planes and the dislocations observed on the (001) plane of the crystal.

In addition to the cube slip (dislocations type a), there were many dislocations lying in bands inclined to the foil with an overall band direction of $[100]$ (type b dislocations). Mixed dislocations lying in bands on the (101) appear to have $[100]$ line direction due to the intersection angle between the (010) and (101) planes. Therefore, foil sections parallel to the (010) plane reveal these bands of dislocations on the (101) plane with an apparent band direction of $[100]$. These dislocations are believed to have $\langle 100 \rangle$ and/or $\langle 110 \rangle$ burger's vectors. Due to the inability to observe these dislocations out of contrast, it was not possible to unambiguously determine the burger's vectors of these inclined dislocations. Therefore, these type b dislocations do not appear on figure 21.

A standard TEM foil for a $g \cdot b = 0$ analysis of the off-stoichiometric Ni-48Al and Ni-52Al was prepared, although the procedure was not performed for these compositions. Both the Ni-48Al and Ni-52Al displayed similar dislocation substructures to that of the Ni-50Al. However, as mentioned in the slip trace analysis, the off stoichiometry compositions showed lesser amounts of the $\{110\}$ slip plane dislocations. $\{100\}$ TEM specimens of the off-stoichiometry compositions revealed similar cube slip dislocations with an absence of the large concentrations of inclined dislocations found in the Ni-50Al TEM specimens. The burger's vectors and line directions found in the off-stoichiometry compositions were the same as the Ni-50Al.

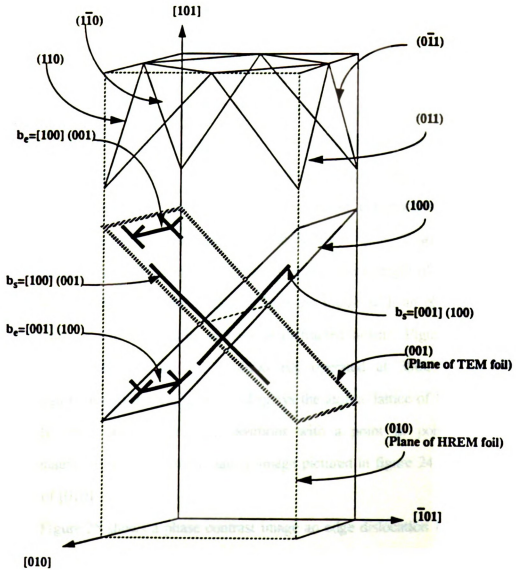


Figure 21: Schematic showing the slip systems activated during compression. The appropriate dislocations are labeled accordingly.

3.4 HREM Observation

Ni-Al sample sections perpendicular to $[100]$ revealed the pure edge dislocations inhabiting the (001) and (010) planes in an 'end on' view. The 'end on' view of these dislocations is necessary for resolution of the core. Dislocations viewed in non-'end on' directions do not reveal the detail of the core and do not provide any information about the core structure. Figure 22 is a diffraction contrast TEM image revealing the 'end on' view point of the cube slip edge dislocations in Ni-50Al at a relatively low magnification. These $\{100\}$ foil sections were imaged in phase contrast to evaluate the fine detail of these $\langle 100 \rangle \{001\}$ edge dislocation core structures for the various compositions of Ni-Al. Phase contrast imaging utilizes the crystallographic nature of the material to provide an image based on constructive and destructive interference of the electron beam with the sample. Figure 23 (a) displays a typical (100) zone with no objective aperture at a nominal camera length of 1.5m. Figure 23 (b) shows the same (100) zone used to form the image with an objective aperture utilizing only a few of the total number of diffracted beams. Figure 24 shows the resolution capability of the JEOL 4000 EX operated at 350kV at a nominal magnification of 600,000X. Figure 24 displays the atomic lattice of Ni-48Al showing the body center and corner atom positions with a point to point resolution of approximately 19 nm. The atomic lattice image pictured in figure 24 (a) has an image normal of $[010]$.

Figure 25 shows a phase contrast image an edge dislocation found in Ni-50Al with a $[100]$ burger's vector on the (001) plane. The line direction (and micrograph normal) of the edge dislocation is $[010]$. The burger's circuit is detailed around the core to illustrate the $[100]$ displacement of the two extra half planes of atoms. It is suggested that the viewer tilt the micrograph so as to view it nearly parallel to the plane of the page to notice the displacements of the regular lattice. The micrograph should be viewed at both right angles to observe the displacements in both directions. By closely



Figure 22: Diffraction contrast micrograph with foil normal of $[010]$. The dark spots represent dislocations with an end on configuration for imaging in phase contrast conditions. The diffracting vector is (101) .



Figure 23 : (a) Diffraction spot pattern of a single crystal thin foil of Ni-50Al, showing a $\{100\}$ zone for the B2 crystal structure with no objective aperture. The additional diffraction spots are created from the superlattice.



Figure 23 : (b) The same $\{100\}$ zone with an objective aperture to limit the number of diffracted beams for phase contrast imaging.

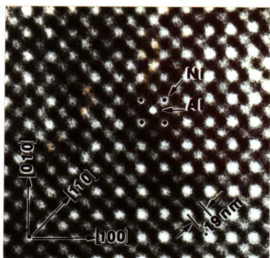


Figure 24 (a): Phase contrast image showing point to point resolution of the regular lattice in Ni-48Al at 350kV accelerating voltage.

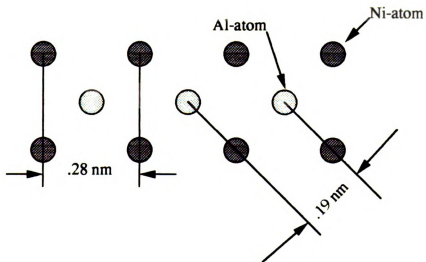


Figure 24 (b): Schematic showing the B2 structure and point to point displacements. The light circles represent Ni-atoms and the dark represent Al.

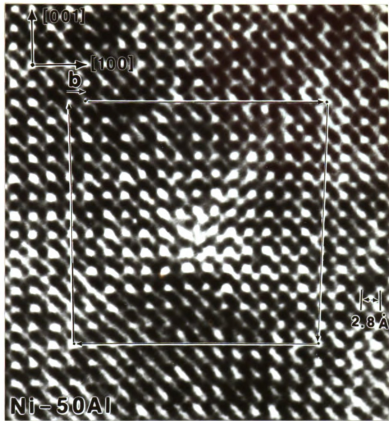


Figure 25: Phase contrast image of a Ni-50Al $[100]$ (001) edge dislocation. The foil normal is $[010]$. The image was taken at 350kV accelerating voltage. .

examining the atomic layers running parallel to the extra two half planes of atoms, it can be seen that there is a considerable amount of disregistry near the core. Examining the atomic layers parallel to the half planes further away from the core one can see that the regiment of the regular lattice is restored. Similarly for the atomic layerings running parallel to the slip plane, or normal to the two extra half planes of atoms, one can observe that again there is considerable displacement out of the slip plane near the dislocation core. As with the displacements parallel to the two extra half planes of atoms, the regiment of the regular lattice is returned in as many as 3 to 4 atomic layerings. This suggests that the displacements of the dislocation core found in Ni-50Al are somewhat localized near the core.

Figure 26 shows a phase contrast image of an edge dislocation found in Ni-48Al with a $[100]$ burger's vector on the (001) plane. The micrograph is taken looking down the $[010]$ zone. The burger's circuit is illustrated around the core of the dislocation to highlight the displacement of extra two half planes of atoms and is again $[100]$. By closely examining the atomic layers parallel to the extra two half planes of atoms, it can be seen that the Ni-48Al core structure is similarly displaced as is the Ni-50Al core. However, the atomic layerings further away from the core still show a significant amount of disregistry whereas the Ni-50Al core was returned to the regular lattice. As many as three or four atomic layers away from the core it can be seen that the Ni-50Al regular lattice is restored whereas in the Ni-48Al the disregistry is still present after as many as six or seven atomic layerings. Hence, the core structure of the edge dislocation found in Ni-48Al is significantly more spread within the slip plane than the core found in Ni-50Al. Similarly, the atomic layings running parallel to the slip planes show a considerable amount more displacement out of the slip plane as well. Again, the Ni-48Al layerings running parallel to the slip plane still display a significant amount of displacement as many as six or seven rows away from the core whereas the Ni-50Al layerings are more uniform after three or four rows away from the core. It is evident

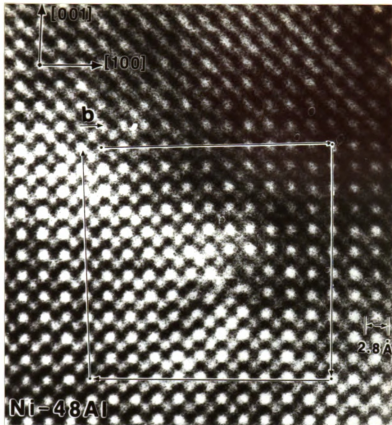


Figure 26: Phase contrast image of a Ni-48Al [100] (001) edge dislocation. The foil normal is [010]. The image was taken at 350kV accelerating voltage

that the core of the cube slip edge dislocation found in Ni-48Al is significantly more spread both in and out of the slip plane than the Ni-50Al core.

Figure 27 shows a phase contrast image of an edge dislocation found in Ni-52Al with a [100] burger's vector on the (001) plane. The direction of micrograph normal is perpendicular to the (010) plane. Again, the burger's circuit is sketched around the core of the dislocation to illustrate the displacement of the two extra half planes of atoms. Although the resolution for this micrograph is not as good as the other compositions, it can be seen that by closely examining the atomic layers running parallel to the two extra half planes of atoms, there is a significant amount of displacement in the slip plane found in the Ni-52Al, similarly to that of the Ni-50Al and Ni-48Al. By examining the atomic layerings running parallel to the slip plane it can be seen that there is a substantial amount of displacement out of the slip plane as in the Ni-48Al core structure. Atomic layerings as far away from the core as six or seven layers still show a significant amount of disregistry, whereas in the Ni-50Al core structure the displaced layers were closer to the core (three or four layers). Similarly to the Ni-48Al, the Ni-52Al core structure is significantly more relaxed both within the slip plane and out of the slip plane. In comparing the core structures of the cube slip ($\langle 100 \rangle \{001\}$) edge dislocations found in Ni-48Al, Ni-50Al and Ni52Al, it is apparent that the off stoichiometric compositions display a more significant spreading of the core than the stoichiometric composition, with the "out of slip plane" distortions being the most prominent.

As was stated in the slip trace analysis section of this investigation, there were significant traces for planes other than $\{100\}$. Although the off stoichiometric compositions displayed a predominance of $\{100\}$ slip plane activation, there was noticeable $\{110\}$ slip plane activation as well. It is not entirely clear what burger's vectors were present in the off stoichiometry compositions because no $g \cdot b = 0$ analysis was performed. However, it has been previously reported that both $\langle 100 \rangle$

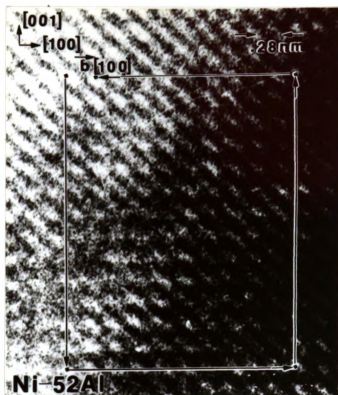


Figure 27: Phase contrast image of a Ni-52Al [100] (001) edge dislocation. The foil normal is [010]. The image was taken at 350kV accelerating voltage.

and $\langle 110 \rangle$ burger's vectors have been observed in the various compositions of Ni-Al [11]. Therefore, the possibility of observing non- $\langle 100 \rangle$ burger's vectors is not high, but not impossible. Figure 28 shows a phase contrast image of a $[110] (001)$ edge dislocation found in Ni-51Al. The burger's circuit is drawn around the core to illustrate the $[110]$ displacement of the two extra half planes. By examining the core's two extra half planes, it can be seen that the two half plane's termination points are separated by one plane of atoms, normal to the two half planes. There is a minor climb dissociation between the termination points of the two half planes of atoms. Portions of the micrograph do not exhibit good resolution, however, the image quality near the core is good enough to examine the structure. Unfortunately, this investigation yielded no other HREM micrographs from the other compositions displaying this $\langle 110 \rangle$ dislocation. A comparison of the relaxation of the core similar to that of the $\langle 100 \rangle \{001\}$ dislocation could have further illustrated this core spreading effect with changes in stoichiometry.

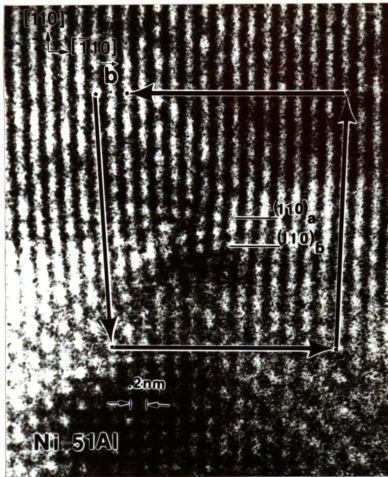


Figure 28: Phase contrast image of a $[110]$ edge dislocation found in Ni-51Al. The burger's circuit is diagramed around the core to illustrate the displacement. The dislocation is slightly climb-dissociated. The termination points of the two extra half planes are labeled a and b.

4. Discussion

4.1 Mechanical Properties

Figure 6 displays the hardness-composition trends of Ni-Al, Co-Al and Fe-Al alloys tested at a 200°C [16]. Ni-Al and Co-Al single crystals with compositions away from the perfect stoichiometry have significantly higher hardnesses than the stoichiometric composition. Additional investigations [6, 7, 11, 45] have reinforced these findings, as well as showing higher yield strengths and lower strain to failure for these Ni and Al-rich compositions. It has been suggested that the increasing hardness and strength with deviations from perfect stoichiometry can be attributed to an increase in the number of point defects in the lattice [34]. This increased number of vacancies is the result of ordering constraints corresponding to changes in stoichiometry. The substitution of a vacancy onto a lattice site is energetically more favorable than a violation of the order [34]. However, while these increases in vacancy concentration may provide argument for Ni-Al and Co-Al systems, they do not explain why this hardness phenomena does not occur in Fe-Al. Both Ni-Al and Co-Al exhibit substantial increases in hardness for off-stoichiometric compositions in either Al or Co, or Ni-rich compositions, whereas Fe-Al actually displays a decrease in hardness for Fe-rich compositions (fig. 6) [16]. The shift in preferred slip plane in the (101) deformed Ni-Al observed in this investigation may help explain this phenomena. The shift from {110} preferred slip for Ni-50Al to {100} for off-stoichiometric compositions coincides with the increasing hardness with composition deviations.

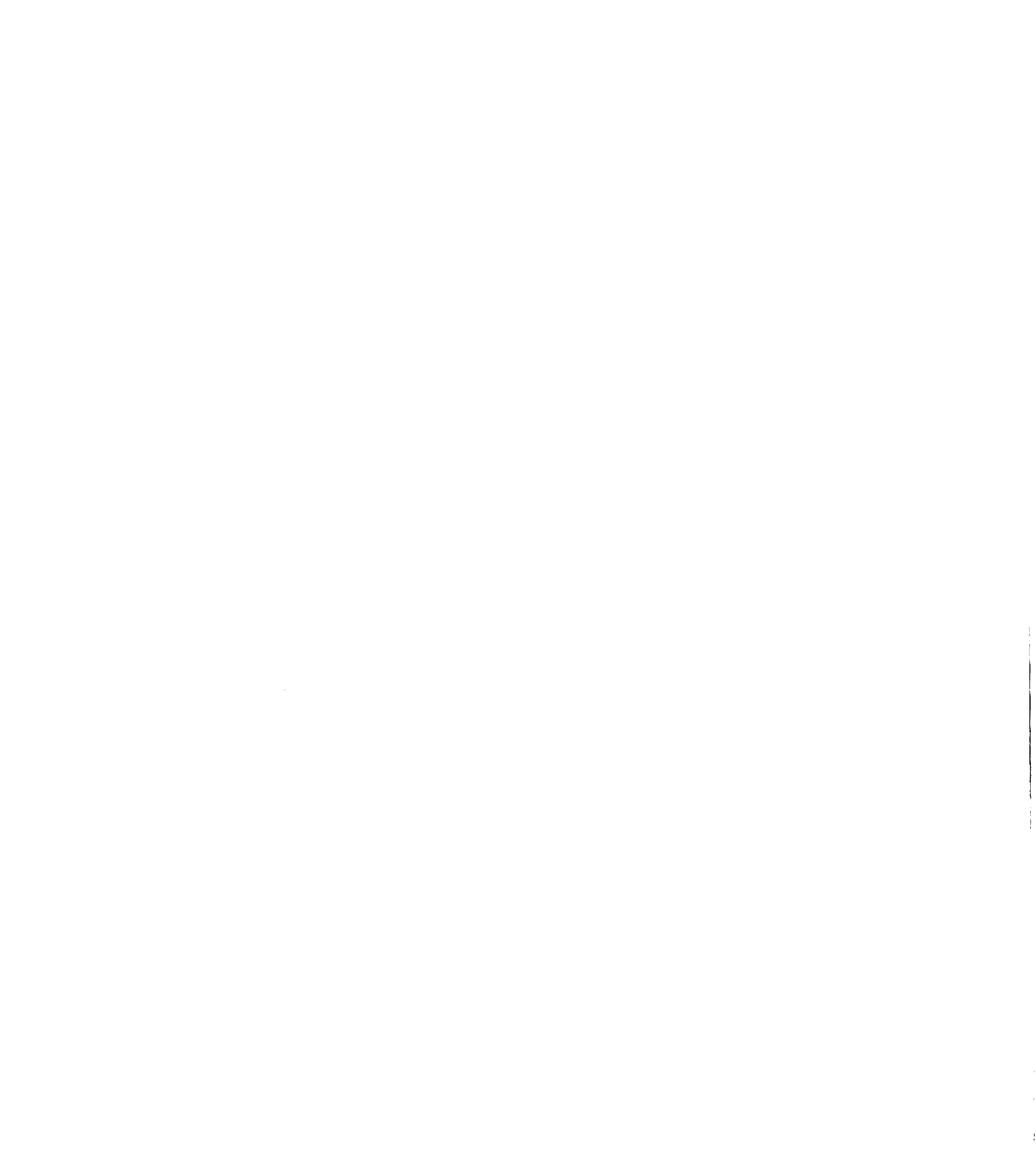
The results of the present study suggest another mechanism for this observed change in hardness and strength with stoichiometry variations. By examining the stereographic projection (fig. 16 (a)) it can be seen that for the Ni-50Al there were six possible planes for which $\langle 001 \rangle$ slip could occur, four {110} and two {100}, whereas the off stoichiometric compositions basically only had two {100} planes being activated. However, a reduction in the number of active slip planes would not

effectively change the mechanical response of the material, whereas a change in the critical resolved shear stress (CRSS) would. This observation suggests there is a change in the CRSS for the various slip systems as a function of stoichiometry. A change in the CRSS values for the various slip systems may also explain this shift in active slip planes. Thus the CRSS for $\{110\}$ slip maybe increasing relative to the CRSS for $\{100\}$ slip as the composition is shifted from Ni-50Al to either a Ni or Al-rich composition. This poses another question as to why the CRSS values are different with changes in stoichiometry. One possibility could be that there is a change in defects that govern the initiation of plastic flow, specifically dislocations. The observed shift preferred slip plane, and consequently hardness, may be described by the nature of the dislocation core structure as a function of stoichiometry. The results of this investigation show that there is a considerable change in the nature of the core of the $\langle 100 \rangle \{001\}$ edge dislocation found in Ni-Al as a function of stoichiometry. This may help explain the increasing hardness with stoichiometry changes.

4.2 Dislocation Core Spread

The observed spread of the $\langle 100 \rangle \{001\}$ edge dislocation core as a function of stoichiometry may help explain the increasing hardness phenomena in Ni-Al alloys. The core of the Ni-50Al, which exhibits the lowest hardness, is somewhat more compressed near the core than the off stoichiometry compositions. The off-stoichiometry Ni-48Al and Ni-52Al display a more relaxed core for these dislocations. This relaxation of the core as a function of stoichiometry should affect the CRSS for these dislocations.

This width, W , of a dislocation is a measure of the lattice distortion associated with the introduction of a dislocation into a perfect lattice [46]. The term W is defined as the distance across the core of the dislocation such that the displacement of the regular lattice is greater than or equal to one fourth of the burger's vector. The Peierls-



Nabarro stress (τ_{p-n}) dependence on the dislocation width and the burger's vector b is given as [47]:

$$(1) \quad \tau_{p-n} = G e^{-2\pi W/b}$$

Where G is the shear modulus. The observed increased width of the off stoichiometry composition's relaxed dislocation core would effectively lower the CRSS. Figure 29 displays a hypothetical edge dislocation core with an effectively small core width, the subsequent plots below the illustration detail the disregistry, Δu , and burger's vector distribution f respectively. Figure 30 is a similar figure 29 with the same burgers vector except that the atomic positions are for a wider core structure.

Based on this argument, the dislocation core observed in Ni-50Al should be more difficult to move than the core observed in Ni-48Al and Ni-52Al. This is contradictory to the mechanical properties reported in the literature [6, 7, 11, 12, 16]. However, the displacements normal to the slip plane may affect the CRSS even more. It is important to note that the above model does not consider displacements normal to the slip plane. The distortion out of the slip plane should make these dislocations harder to move. Such as the case with the $\langle 111 \rangle$ screw type dislocations found in bcc type materials. The three fold symmetry must first be compressed into a planar core before the dislocation can be set in motion. Hence, more stress should be required. Figure 31 is a digitized image of the Ni-50Al edge dislocation pictured in figure 25. The digitized image has been elongated in the vertical direction and compressed in the horizontal to better examine the spread of the core out of the slip plane. This type of image illustrates the effect of examining the 'tilted' image to look down the planes in the compressed direction. Figure 32 is similar to figure 31 but for the off stoichiometric Ni-48Al composition showing the distortions out of the slip plane are greater for this alloy. These two figures help illustrate this increased spreading out of the slip plane

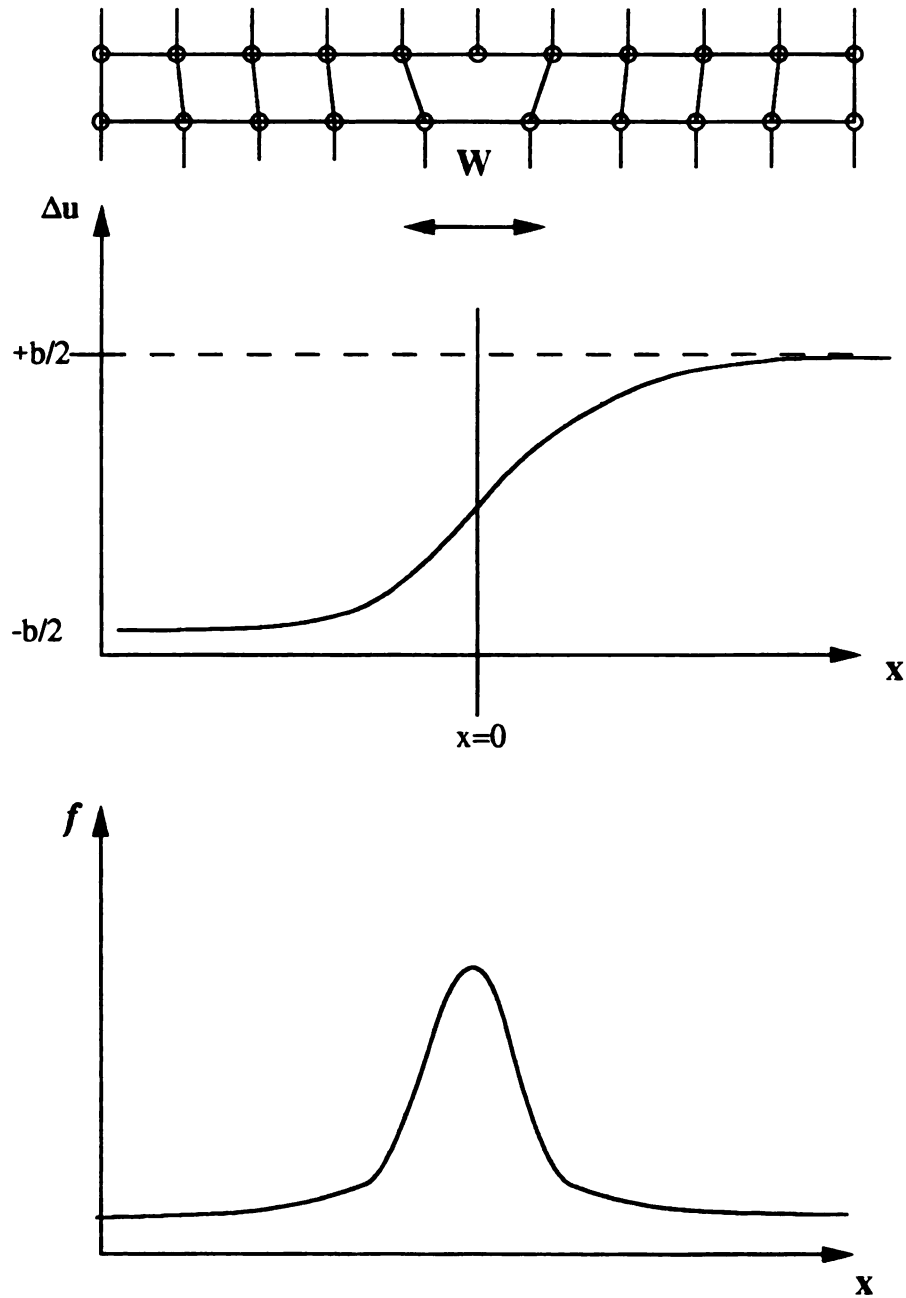


Figure 29: Schematic of an edge dislocation core showing atomic positions for relatively locally compressed configuration. The subsequent plots below the illustration detail the disregistry, Δu , of the regular lattice and the burger's vector distribution function, $f=d(\Delta u)/dx$.

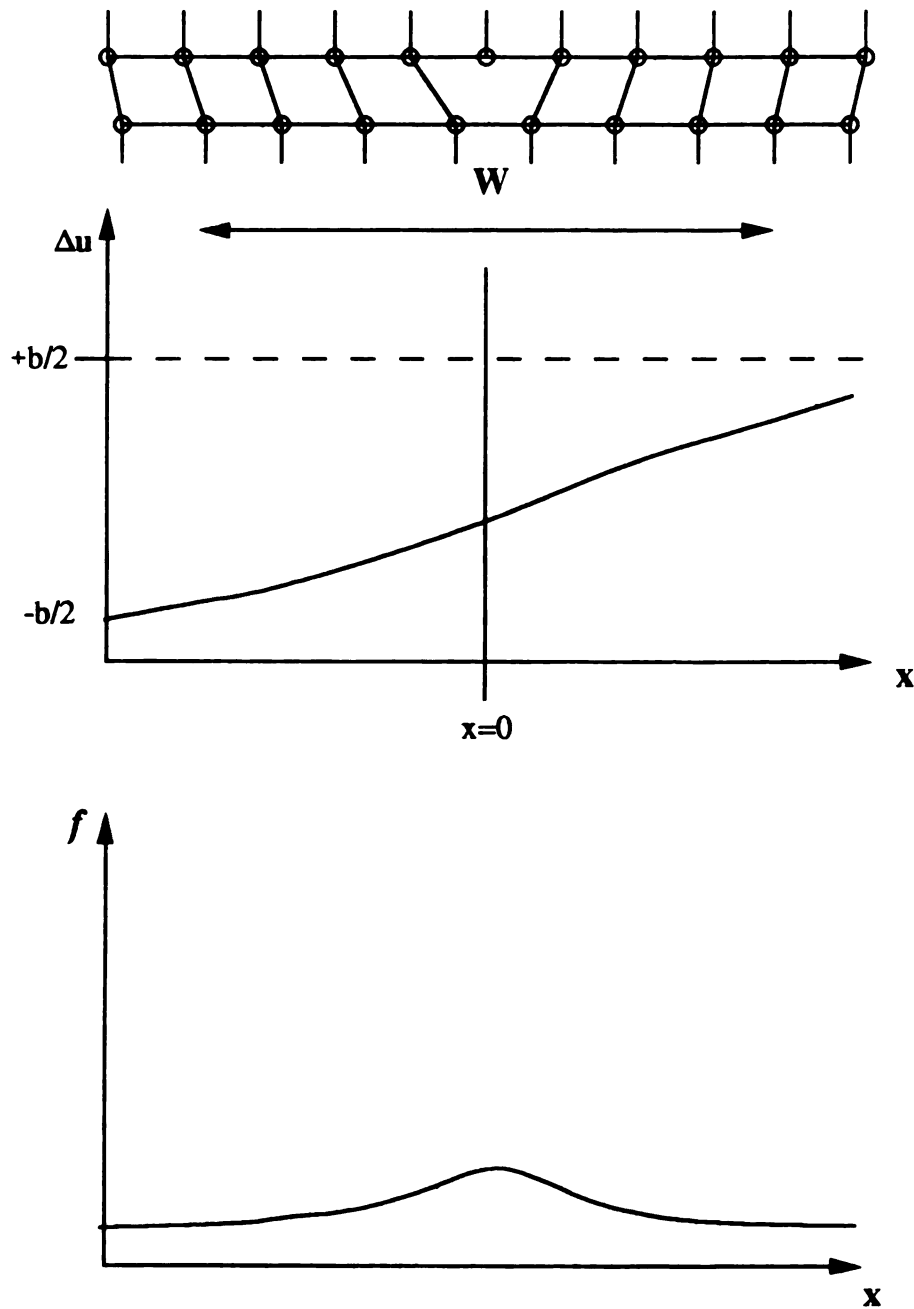


Figure 30: Schematic of an edge dislocation core showing atomic positions for a spread configuration. The subsequent plots below the illustration detail the disregistry, Δu of the regular lattice and the burger's vector distribution function, $f=d(\Delta u)/dx$.

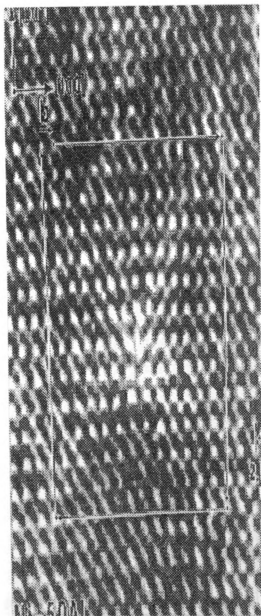


Figure 31: Digitized image of the Ni-50Al core structure originally pictured in figure 25. The core image has been elongated to better illustrate the displacement out of the slip plane.

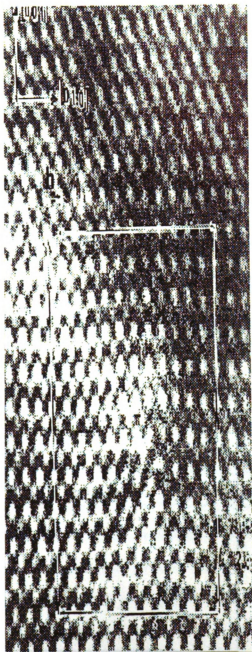


Figure 32: Digitized image of the Ni-48Al core structure originally pictured in figure 26. The core image has been elongated to better illustrate the displacement out of the slip plane.

with a 2 at.% Ni-rich shift in composition away from stoichiometric Ni-50Al. Hence, this relaxation of the core out of the slip plane in these $\langle 100 \rangle \{001\}$ edge dislocations in Ni-48Al and Ni-52Al would require greater stress to move them. This increased stress needed for the off stoichiometric compositions would effectively result in a higher CRSS and a higher overall material strength. Conversely, Ni-50Al's dislocation core that is less displaced out of the slip plane would require a lower stress to move [20, 46, 47]. These core differences help explain the observed mechanical responses of the material as a function of stoichiometry.

Even though these edge dislocations are harder to move in Ni-48Al and Ni-52Al, these compositions exhibit more of these $\langle 100 \rangle \{001\}$ dislocations than the Ni-50Al, indicating that these dislocations become the dominant dislocation with changes in stoichiometry. This implies that while these dislocations are becoming more difficult to move, relative to the other dislocation types (namely $\langle 001 \rangle \{110\}$), they are becoming easier to move. Thus it is possible that the core spreading processes which governs the dislocations on the $\{100\}$ planes is more pronounced on the $\{110\}$ slip systems. It would be of great interest to examine these dislocations on the $\{110\}$ slip planes using HREM in a similar manner as the $\{100\}$ analysis performed in this investigation. However, as mentioned earlier in the procedure section, this analysis does not have a good potential for success due to the resolution limits of the microscope. The problem imposed by using HREM for the $\langle 011 \rangle \{110\}$ dislocations is that the line direction of these dislocations is $\langle 101 \rangle$, therefore the interatomic spacings on the $\{101\}$ are below the resolution capability of the microscope. However, it can be deduced that likely there are probable dramatic changes in the cores of the dislocations on the $\{110\}$ planes which are affecting their mobility and consequently increasing the hardness of the material by making these $\langle 011 \rangle \{110\}$ dislocations more difficult to move.

4.3 Computer Simulation of HREM images

To facilitate a comparison with theoretical work, computer models of the $\langle 100 \rangle \{001\}$ edge dislocation were supplied by Pasianot et. al. [29]. These theoretical core models were generated using the Embedded Atom Method (EAM). The EAM model uses what is known as a supercell of several thousand atoms and calculates the most energetically favorable configuration of a defect (dislocation) within this supercell based on interatomic potentials. In order to compare experimental observations of the actual dislocations found in the material to the theoretical model's images of the theoretical cores, the model cores had to be simulated under HREM conditions. The HREM simulation of these core models was performed using the EMS HREM simulation software package [44]. The EMS software simulates what the model dislocation core will look like under phase contrast conditions given the various parameters; aperture size, accelerating voltage, spherical aberration, specimen drift, astigmatism, deviation off the zone, voltage fluctuations or spread, defocus and foil thickness. Deviations in the last two of this group have dramatic effects on the appearance of the simulated core structure. Figure 33 shows how differences in foil thickness change the nature of the HREM simulation. Notice how the positions that were once white spots that represented atoms for a thickness of 2.871nm, appear as dark spots for a thickness of 11.484 nm. Note in particular, thicker areas only exhibit super lattice resolution. Only by close comparison of the computer model to the simulated HREM image of the model can these assignments of white spot and dark spot for atomic positions be made. This illustrates the need for HREM image simulation when analyzing the experimental images. Figure 34 displays the dislocation core structure simulation for a variety of different defocus conditions. It can be seen that minor deviations in the defocus dramatically change the appearance of the simulated image similarly to that of the foil thickness variation. Both of the simulation series are

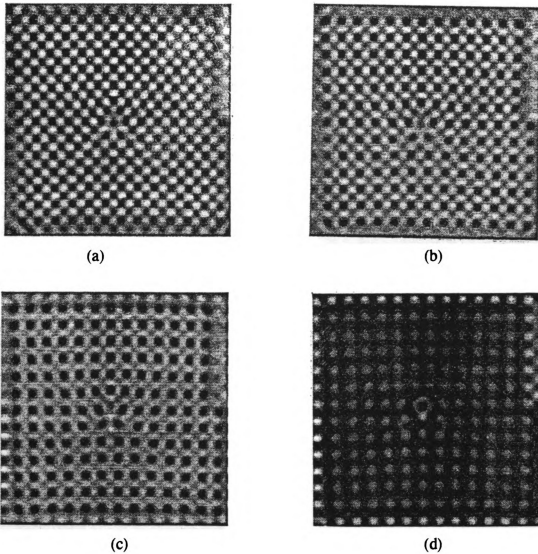


Figure 33: HREM simulations showing the effect of thickness changes. The defocus is 60 nm. The thickness values are (a) 2.871nm, (b) 5.741 nm, (c) 8.613 nm, and (d) 11.484 nm.

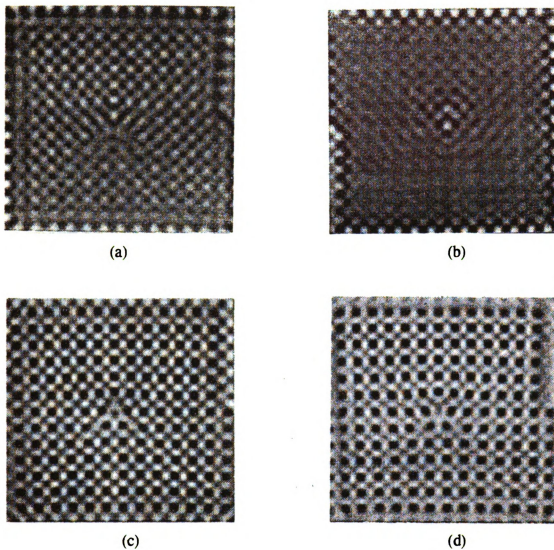


Figure 34: HREM simulations showing the effect of defocus. The foil thickness is 7.17 nm. The defocus values are (a) 40nm, (b) 45 nm, (c) 55 nm, and (d) 60 nm.

near the Scherzer condition. This observed change in image appearance is crucial in comparing the experimental images to the EAM model.

4.4 Dislocation Core Structure

It is interesting to know the basic structure of the $\langle 100 \rangle \{001\}$ dislocation core as well as other dislocations. Figure 35 (a) and (b) shows projected potentials for two possible core configurations for the $\langle 100 \rangle \{001\}$ edge dislocations found in Ni-50Al produced by the EAM[29]. The projected potential represents the charge densities of the supercell and shows the actual atom positions used in the simulations. The difference between the two core structures is that the extra two half planes of atoms associated with the $\langle 100 \rangle$ edge dislocation, can either terminate on a Ni or Al site. The core structure with the two half planes terminating on the aluminum atom site appears to have a more 'asymmetric' shape than does the core structure of the two half planes terminating on the Ni site. Figure 36 is an illustration to gain a better understanding of what the two different cores look like (note: this is merely an illustration to better show the difference between the two structures). It is important to mention that according to the EAM model, both of the theoretical dislocation core structures in figure 35 (a) and (b) are possible. However, the only core configurations observed experimentally were that of figure 35 (a), or the 'symmetric core'. None of the dislocations observed in this investigation had the 'asymmetric' configuration (fig. 35 (b)).

The experimental image for the Ni-48Al dislocation core also matches the 'symmetric' structure projected potential near the core, although the simulation does not account for this increased spreading both in and out of the slip plane. All of the experimental HREM images observed in this investigation display the basic "symmetric" configuration.

In an attempt to model deviations in stoichiometry, local deviations in core chemistry were calculated and projected for comparison to the experimental images. The model and corresponding projected potentials were adjusted to simulate the off-

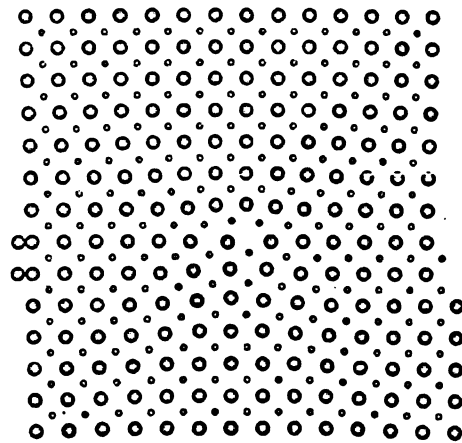
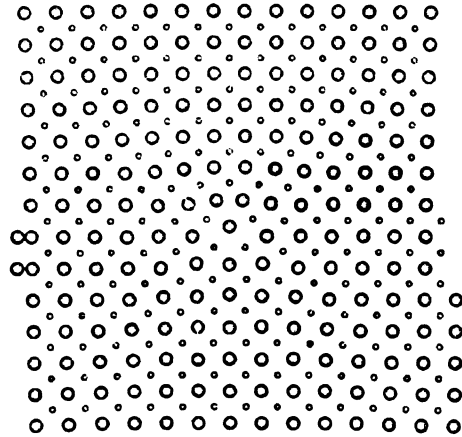


Figure 35: Super cells for two possible $\langle 100 \rangle \{001\}$ Edge dislocations for Ni-50Al. (a) 'symmetric', (b) 'asymmetric'. Adapted from [28].

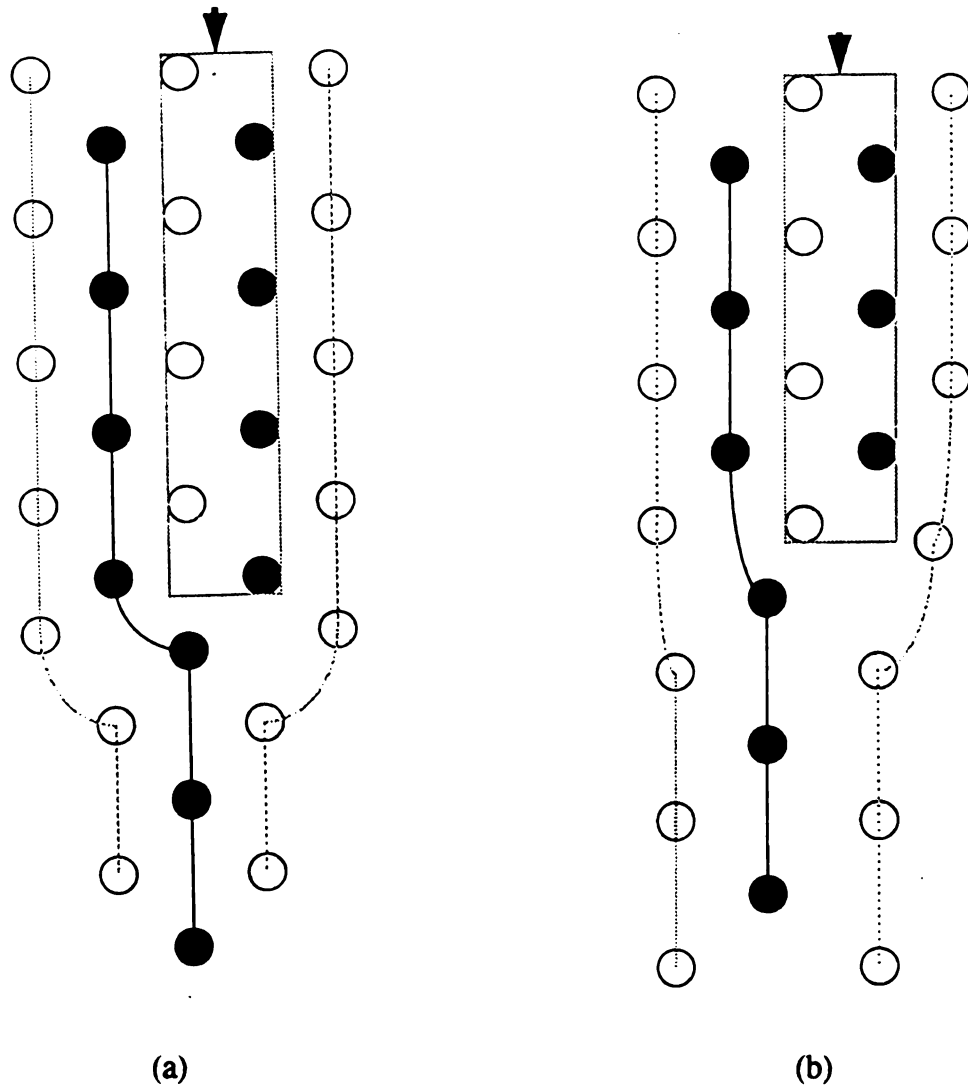


Figure 36: Illustration of the EAM dislocation core models, (a) details the effects of the 'symmetric' core structure and (b) represents the 'asymmetric' core structure. The difference between the two cores is the termination atom of the two extra half plane. The light circles represent Al atoms and the dark circles represent Ni atoms.



stoichiometry effect by making substitutions near the core in the supercell. Once the substitution was made, the equilibrium configuration was calculated and projected. Figure 37 is a series of HREM computer simulations and projected potentials of this dislocation with local changes in stoichiometry. These local deviations in core chemistry do significantly change the projected potential of the model. It is difficult to properly compare such minor fluctuations in the model to that of the experimental images due to the resolution capability of microscope. While the general experimentally observed structure of the core does not change from that of the Ni-50Al, these local variations do not simulate the spreading of the core either within, or normal to the slip plane. Hence, these local changes in the computer modeled core structures do not predict the core structure for the off stoichiometric compositions.

Recently Mills [42] has imaged the $\langle 100 \rangle \{001\}$ edge dislocation core in single crystal Ni-50Al. Comparison Mill's core image to the observed in this investigation reveals similar core structures. Both Ni-50Al core structures appear to have the extra two half planes of atoms terminating on a Ni-atom. The computer simulation [29] used in this investigation compares well to that of Mill's investigation also. Figure 38 shows a $\langle 100 \rangle \{001\}$ edge dislocation from this investigation with somewhat poorer resolution at a slightly lower magnification. By examining this dislocation core approximately 45 degrees in either direction of the two extra half planes it can be seen that there are two apparent single half planes residing on the $\{110\}$ planes. This observation is in good agreement with Mill's findings and the computer model used to project the theoretical core structure of this dislocation.

The observed $[110]$ edge dislocation in this investigation differs significantly to that of Mill's investigation [42]. Figure 28 displays a phase contrast image of a slightly climb dissociated $\langle 110 \rangle$ burger's vector edge dislocation found in Ni-51Al in this investigation. The dislocation in figure 28 is actually two climb-dissociated $1/2[110]$ partial dislocations separated by an climb antiphase boundary. Figure 39 is a schematic

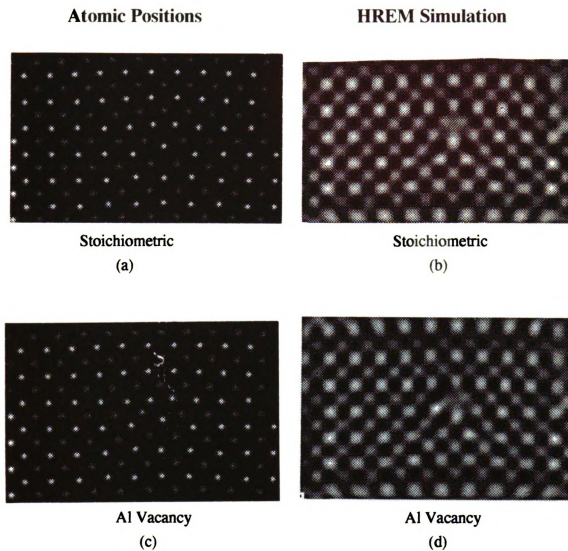
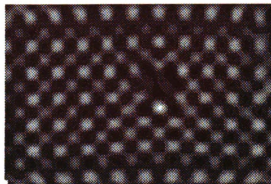


Figure 37: Atomic position maps based on EAM calculations for Ni-50Al, (a), and for local substitution of an Al vacancy (c). (b) and (d) HREM simulations for (a) and (c) respectively.

Atomic Positions

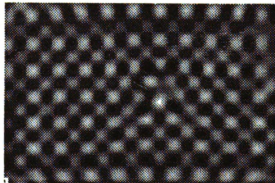
Ni Vacancy
(e)

HREM Simulation

Ni Vacancy
(f)



Extra Al Atom
(g)



Extra Al Atom
(h)

Figure 37 cont. : Atomic position maps based on EAM calculations for a Ni vacancy (e), and for local substitution of an extra Al atom (g). (f) and (h) are HREM simulations of (a) and (g) respectively.

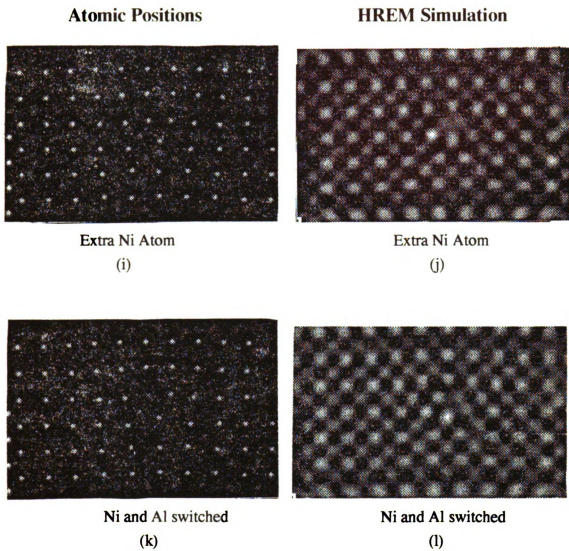


Figure 37 cont. : Atomic position maps based on EAM calculations for an extra Ni atom (i) , and for local switch of an Al with Ni atom (k). (j) and (l) are HREM simulation of (i) and (k) respectively.

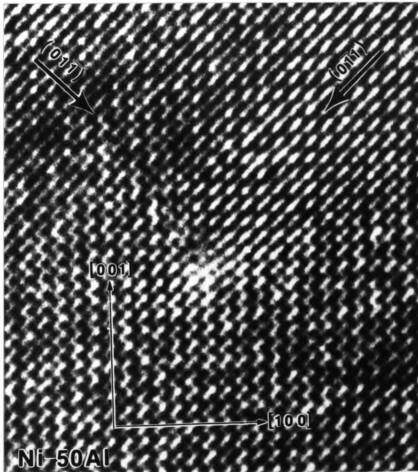


Figure 38: Phase contrast image of a Ni-50Al $[100]$ (001) edge dislocation. The foil normal is $[010]$. The image was taken at 350kV accelerating voltage. The arrows indicate the apparent extra two half planes along the $\{110\}$ planes.

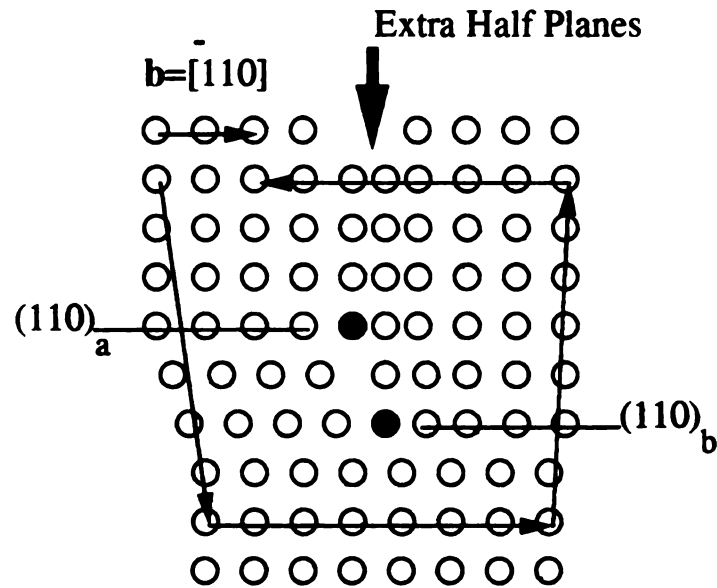


Figure 39: Schematic representation of the dislocation pictured in figure 28. The half plane termination planes are labeled as 'a' and 'b' and the termination atoms are represented as black circles.

representation of figure 28 showing the dissociated pair of dislocations. Close examination of the experimental image reveals the two $1/2[110]$ dislocations actually terminate at two different slip planes separated by a single plane of atoms. Mills [42] observed a similar dislocation in Ni-50Al that was significantly more dissociated than the one observed in this investigation. Intuitively, the more dissociated $\langle 110 \rangle$ dislocation observed by Mills may be easier to move than the one observed in this investigation. Comparison between the two cores clearly shows the dissociation effect. Mill's also noted that under high resolution conditions these dissociated $\langle 110 \rangle$ dislocations decomposed under the energy of the beam into $\langle 100 \rangle$ dislocations. However, the slightly climb dissociated core in figure 28 did not decompose into $\langle 100 \rangle$ dislocations.

There were several observations of $\langle 110 \rangle$ dislocations with varying structures found in the Ni-51Al results. Unfortunately, not all of the images proved useful due to the inability to get the maximum regular lattice resolution. Several single $1/2\langle 110 \rangle$ dislocations were observed without the accompanying $1/2\langle 110 \rangle$ partial and antiphase boundary. It has long been known that these single $1/2\langle 110 \rangle$ dislocations cannot exist alone for they are a disordering dislocation and need a second dislocation with the same burger's vector plus an APB to preserve the order of the bulk. In contradiction, Figure 40 displays one of these single $1/2\langle 110 \rangle$ dislocations in Ni-51Al. There are a couple possible explanations for this single dislocation. One line of conjecture could be that this dislocation is an edge component of a $\langle 111 \rangle$ mixed dislocation. However, this is not possible because the resolved edge component of a $\langle 111 \rangle$ mixed dislocation has a b direction of $\langle 110 \rangle$ when observed down a $\langle 001 \rangle$ zone. The line direction of this image is $\langle 100 \rangle$. Another viable possibility is that this single $1/2\langle 110 \rangle$ dislocation was part of a pair of partial dislocations separated by an APB. Quite possibly one of the super partial dislocations moved out of the foil while the one observed was left behind as a sessile remnant, but this not easily rationalized because of the high APB energy in

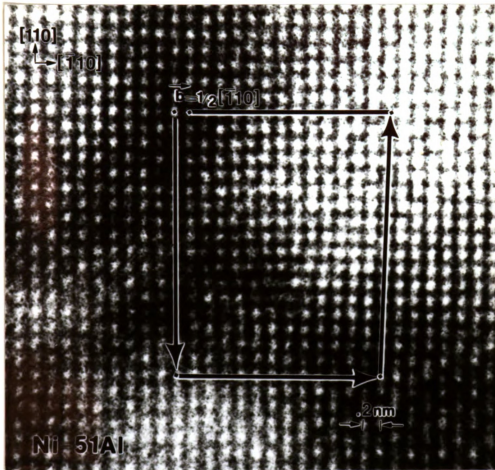


Figure 40: Phase contrast image of an apparent $b=1/2[110]$ edge dislocation in Ni-51Al. This image was taken at an accelerating voltage of 350 kV.

Ni-Al. Initially this image was thought to be a superlattice resolution image of a $\langle 100 \rangle$ or $\langle 110 \rangle$ dislocation. Recall that the superlattice is visible in thicker regions of the sample, thus a $\langle 100 \rangle$ in the regular lattice would appear as a $1/2\langle 110 \rangle$ in the superlattice. However, close calibration of the 'white dot' spacings and careful examination of the negative from which this image was obtained from, proved this image to be an actual regular lattice resolution image. The diffraction intensity differences between the apparent Ni and Al atoms further supports the hypothesis that this is a regular lattice image. Hence, the argument of poor resolution does not apply. Therefore, this image cannot be all inclusively defined.

5. Conclusions

Stoichiometric Ni-50Al displayed predominantly $\{011\}$ slip planes with limited $\{001\}$ slip plane activation for the $\langle 101 \rangle$ oriented single crystals deformed in compression at 400°C. The off stoichiometric Ni-52Al and Ni-48Al displayed mostly $\{001\}$ slip with limited $\{011\}$ slip plane activation when deformed under similar conditions. This illustrates that there is a change, as a function of stoichiometry, in the preferred slip plane for the $\langle 101 \rangle$ orientation. A change in the critical resolved shear stress for the dislocations on these slip planes is influencing the dislocation slip properties of the material.

The $\langle 100 \rangle \{001\}$ edge dislocation core structure of the Ni-50Al is somewhat compressed with respect to relaxations within the slip plane. There are substantial displacements out of the slip plane also, which help explain the hard nature of Ni-Al in general. The Ni-48Al and Ni-52Al have a more relaxed core structure within the slip plane than the stoichiometric Ni-50Al. This is contradictory to the observed mechanical properties based on the relationship between core relaxations and critical resolved shear stress. However, the greater displacements out of the slip in the core of these dislocations in the off stoichiometric compositions would influence the dependence of the CRSS even more. It is likely that the dislocations on the $\{110\}$ planes are being affected by these displacements out of the slip plane to a greater degree, which in turn causes the $\{100\}$ slip planes to become the dominant plane of slip for the off stoichiometric compositions.

The theoretical model used in this investigation predicts the basic core structure of the $\langle 100 \rangle \{001\}$ edge dislocation for the stoichiometric Ni-50Al. However, the projected potential does not take into account the displacements out of the slip plane for the Ni-50Al or the off stoichiometric Ni-48Al and Ni-52Al. Furthermore, the deviation

of local core chemistry does not accurately predict the spreading of the core within the slip plane as a function of stoichiometry either.

REFERENCES

1. R. Darolia, JOM, 1991, March, p.44.
2. S. V. Raj, Met. Trans. 1992, 23A, p. 1691.
3. N. J. Zaluzec, H. L. Fraser, Scr. Met., 1974, 8, p. 1049.
4. P. R. Monroe, I. Baker, Scr. Met., 1989, 23, 495.
5. A. Ball, R. E. Smallman, Act. Met., 1966, 14, p. 1517.
6. J. D. Whittenberger, NASA TM 83006, NASA-Lewis Research Center, Cleveland, OH, 1982, p. 163.
7. J. H. Westbrook, Mechanical Properties of Intermetallic Compounds, 1960, John Wiley and Sons, New York, NY, p. 1.
8. F. N. Rhines and J. B. Newkirk, Trans., ASM, 1953, 45, 1029.
9. P. Nash, M. F. Singleton and J. L. Murray, Phase Diagrams of Binary Nickel Alloys, 1991, 1, ASM international, Metals Park, OH.
10. G. Sauthoff, Mechanical Properties of Intermetallics at High Temperatures, High Temperature Aluminides and Intermetallics, 1989, TMS, p. 329.
11. R. J. Wasilewski, Metall. Trans., 1966, 236, p. 455.
12. D. F. Lahrman, R. D. Field and R. Darloia, High Temperature Ordered Intermetallic Alloys IV, 1991, MRS.
13. L. A. Kuchererenko and V. A. Troshkina, Izvest. Akad. Nauk. SSSR Metally, 1971, 1, p. 115.
14. J. D. Whittenberger, NASA N 83 11300 D18, NASA-Lewis Research Center, 1982, p. 163.
15. W. D. Nix, NASA N83 11302 D20, NASA-Lewis Research Center, 1982, p. 183.
16. J. H. Westbrook, J. Electro. Chem. Soc., 1956, V. B, p. 54.

17. L. A. Hocking, P. R. Strutt, and R. A. Dodd, *J. Met.*, 1971, 99, p.98.
18. J. W. Christian, *Met. Trans.*, 1983, 14A, p. 1237.
19. V. Vitek, R. C. Perrin, and C. K. Bowen, *Phil. Mag.*, 1970, 21, p. 1049.
20. V. Vitek, *Scripta Met.*, 1970, 4, p. 725.
21. Z. S. Basinski, M. S. Duesbury, and R. Taylor, *Phil. Mag.*, 1970, p. 1201.
22. Z. S. Basinski, M. S. Duesbry, and R. Taylor, *Can. J. Phys.*, 1971, 49, p. 2160.
23. M. Yamaguchi, *Mechanical Properties of bcc Metals*, M Meshii ed., AIME, 1981, p. 31.
24. S. Takeuchi, *Phil. Mag.*, 1980, 41A, p. 541.
25. M. Yamaguchi and Y. Umakoshi, *The Structure and Properties of Crystal Defects*, V. Paidar and L. Lejcek eds., *Materials Science Monographs*, 20, p. 131.
26. S. Takuchi, *Mechanical Properties of bcc Metals*, M. Meshii ed., AIME, 1981, p. 17.
27. V. Vitek, *Dislocations and Properties of Real Materials*, *Inst. of Met.*, London, 1985, p. 30.
28. T. A. Parthasarathy, S. I. Rao and D. M. Dimiduk, *Phil. Mag.*, submitted May 12, 1992.
29. R. Pasianot, D. Farkas and E. J. Savino, *J. Phys. III*, 1991, 1, p. 997.
30. M. Yamaguchi and Y. Umakoshi, *Scripta Met.*, 1975, 9, p. 637.
31. E. M. Schulson and E. Teghtsoonian, *Phil. Mag.*, 1969, 19, p. 155.
32. D. L. Yaney and W. D. Nix, *J. Mat. Sci.*, 1988, 23, p. 3088.
33. A. G. Rozner and R. J. Wasilewski, *J. Inst. Met.*, 1966, 94, p. 169.
34. K. H. Hahn and K. Vedula, *Scripta Met.*, 1989, 23, p. 7.
35. R. Darolia, D. F. Lahrman, R. D. Field and A. J. Freeman, *High Temperature Ordered Intermetallic Alloys III*, C. T. Liu, A. I. Taub, N. S. Stoloff and C. C. Koch eds., *MRS sym. Proc.*, 1989, 133, p. 113.
36. J. D. Whittenberger, *Mat. Sci. and Eng.*, 1985, 73, p. 87.
37. J. D. Whittenberger, *Mat. Sci. and Eng.*, 1987, 85, p. 91.
38. R. J. Wasilewski, S. R. Butler, J. E. Hanlon, *Trans. AIME*, 1967, 239, p. 1357.

39. P. R. Bowman, R. D. Noebe, and R. Darloia, in prep.
40. D. B. Miracle, *Acta Met. Mater.*, 1991, 39, No. 7, p. 1457.
41. M. A. Crimp, *Phil. Mag. Letters*, 1989, 60, No.2, P. 45.
42. M. J. Mills and D. B. Miracle, *Acta Met. mater.*, 1993, 41, No. 1, p. 85.
43. B. D. Cullity, Elements of X-Ray Diffraction, second ed., Addison-Wesley Publishing co., Reading Mass., 1978.
44. M. J. Mills, Computer Simulation of Electron Microscope Diffraction and Images, W. Krakow and M. O'Keefe eds., 1989, *The Minerals, Metals and Materials Soc.*, p.239.
45. A. Lasalamonie, *J. of Mat. Sci.*, 1982, 17, p. 2419.
46. F. R. N. Nabarro, *Proc. Phys. Soc.*, 1947, 59, p. 256.
47. R. Pierels, *Proc. Phys. Soc.*, 1940, 52, p.34.

MICHIGAN STATE UNIV. LIBRARIES



31293008927232